Analysis Note for $\gamma p \rightarrow p\phi\eta$

Bradford E. Cannon

April 9, 2018

Table of Contents

1 Selecting $\gamma p \rightarrow p\phi\eta$ Events at GlueX

In order to study potential states of bound strangeonia, it is essential to properly identify all final and initial state particles. The final state topology that will be studied for this thesis is $\gamma p \rightarrow pK^+K^-\gamma_1\gamma_2$, where the K^+K^- pair are daughter states of the ϕ meson, and the $\gamma_1\gamma_2$ pair are daughter states of the η meson. Therefore, the beginning of this analysis section will focus on the particle identification of the proton, kaons, and final state photons, as well as the incident beam and target proton. Once identification of all particles has been well established, this analysis will then investigate whether or not a correlation exists between the ϕ and η bound states. This analysis will be conducted by means of sampling different regions of the $\gamma_1\gamma_2$ invariant mass and the K^+K^- invariant mass. Ultimately, it will be shown that a correlation does in fact manifest itself within this data set, and therefore a thorough strangeonia analysis can be performed.

1.1 Spring 2017 Run Period

The data presented here is the result of the successful Spring 2017 Low Intensity run period. The Spring 2017 run period spanned from January 23rd to March 13th and accumulated roughly 50 billion physics events. The maximum electron beam energy used was 12 GeV, and the accelerator ran at 250 MHz while in low intensity (beam every 4 ns), and later ran at 500 MHz while in high intensity (beam every 2 ns). Upon entering Hall D, the electron beam was incident upon a radiator. During this run period, both amorphous and diamond radiators were used to produce either incoherent or coherent polarized bremsstrahlung radiation. The diamond radiator was experimentally set up to produce linear photon polarization at four different angles; 0°, 45°, 90°, and 135°. These directions were chosen in order to provide the detector with a uniform sampling of linear polarization in the transverse direction to the incident beam. In order to yield roughly the same amount of statistics for an amorphous radiator run as compared to a diamond radiator run, a beam current of 150 nA was incident upon the amorphous radiator, while a beam current of 100 nA was incident upon the diamond radiator. Farther downstream, a 5mm collimator hole was used for all radiator configurations. Lastly, the collimated photon beam was incident upon a stationary liquid hydrogen target. This resulted in one petabyte of files and $16pb^{-1}$ of integrated luminosity.

1.2 Particle Identification

Once all of the data files were written to disk, an analysis launch was initiated. Part of this analysis launch searched for the $\gamma p \to pK^+K^-\gamma\gamma$ topology and incorporated a kinematic fitter which simultaneously constrained four momentum and a common production vertex for the final state particles. It should be noted that this analysis did not enforce the K^+K^- pair come from a ϕ parent state, or the $\gamma\gamma$ pair come from an η parent state; even though the ultimate goal of this analysis is to study the parent states of $\phi\eta$. After successful completion of the analysis launch, the data was then processed by a DSelector which applied several cuts to the data. Initial cuts on the data included timing cuts in the Barrel Calorimeter (BCAL), Forward Calorimeter (FCAL), and the Time of Flight detector (TOF). These timing cuts were made for all of the final state particles ($p, K^+, K^-, \gamma_1, \gamma_2$). A table of the timing cuts used for each final state particle and its associated detector apparatus is given in Table 1. An in depth explanation of these cut values and how they were chosen is provided in the subsection 3.2.

A list of timing plots for all of the final state particles and detector systems is given in Figures 1234. In these Figures, the top plot includes timing measurements from the BCAL, the middle plot includes timing measurements from the FCAL, and the bottom plot includes timing measurements from the TOF. All plots have the timing on the vertical axis and the measured magnitude of the three momentum on the horizontal axis. The 'z' axis is logarithmically scaled with the relative values given by the color bar to the of the plots. The ΔT measurement comes from comparing the measured timing from the associated detector with the time reported by the RF, or beam. To identify particles, we want to only select candidates that have a ΔT close to zero.

Particle	Detector	ΔT Cut [ns] (2σ)
Proton	BCAL	$\pm$ 0.6
Proton	FCAL	$\pm$ 1.0
Proton	TOF	$\pm$ 0.4
K^+	BCAL	$\pm$ 0.7
K^+	FCAL	$\pm$ 0.8
K^+	TOF	$\pm$ 0.2
K^-	BCAL	$\pm$ 0.7
K^-	FCAL	$\pm$ 0.8
K^-	TOF	$\pm$ 0.2
γ	BCAL	$\pm$ 1.0
γ	FCAL	$\pm$ 1.1

Table 1: A table with timing cut values for all final state particles in the reaction $\gamma p \to pK^+K^-\gamma_1\gamma_2$. The values of the timing cuts change depending on both the particle species and detector system resolution. It should be noted that the final state photons only have the calorimeters as possible timing detectors. This is due to the fact that they do not interact with the TOF detector.

After the timing cuts for all of the final state particles was performed, additional cuts were made to identify the $\gamma p \rightarrow pK^+K^-\gamma_1\gamma_2$ final state. One of these cuts included enforcing the reconstructed vertex for all final state particles to be within the geometric volume of the target chamber. Since this analysis does not contain a particle lifetime which would result in a detached vertex, it is imperative to remove backgrounds from other channels that may have this feature, such as excited baryons with a strange quark. An example of what the reconstructed vertex for the final state photons looks like in the z direction (along the beam direction) and in the x-y plane (transverse to the beam direction), as well as the associated cut values, is given in Figure 5.

Another additional cut that is made on the data pertains directly to the identification of the correct beam photon bunch. Since the electron beam is delivered from the accelerator every four nanoseconds, the timing of when the particles arrive into the hall is well known and we call the the Radio Frequency (RF) time. However, once the photons are in the hall, it is unclear which beam bunch may have caused the subsequent physics event. When a physics event takes place, there is an associated beam time which is recoded by either the tagger hodoscope or the tagger microscope. This device can measure both the energy of the beam and the timing of the beam. One of the cuts is made on the the data presented is the difference between the recorded beam time and the reported RF time. An example of what this data looks like and the cut used for it is given in Figure 6.

The last cut that was performed by the DSelector was the value of the observed beam energy. Although this cut does not technically fall under the category of a particle identification, it is included in this section because it was used as a prerequisite for the rest of this analysis. Since this study will ultimately focus on a reaction which requires a high 't' momentum transfer, it is natural to only allow beam photons with high momentum to begin with. This, coupled with the fact that low energy photons produce low statistics for this channel, is the reason why a beam energy cut of $Beam_E \geq 7.5$ GeV was enforced early in the analysis. It should also be noted that this analysis will include a beam asymmetry study for strangeonia which will force the beam energy to be within the coherent peak region $(8.0GeV - 8.8GeV)$. An example beam energy distribution with the associated cut is given in Figure 7.

1.3 Kinematic Fit Confidence Level Cut Study

This is where I am... Need to continue editing document from here...The first of the cuts included a kinematic fit confidence level cut of $1x10^{-4}$. This kinematic fit confidence level was chosen based on a study that was performed on this data after it was processed by the analysis launch. In this study, both the η and ϕ peaks from the $\gamma\gamma$ and K^+K^- invariant mass spectra were fitted as a function of kinematic fit confidence level cut. The η peak was fitted with a Gaussian plus a first degree polynomial while the ϕ peak was fitted with a Gaussian plus a second degree polynomial. Examples of an η fit from this study is given in Figure 8, and an example ϕ fit from this study is given in Figure 9. In each figure, the blue line represents the sum of the Gaussian plus the polynomial fits, the green line represents the Gaussian fit, and the red line represents the polynomial fit. Additionally, both figures are the result of a kinematic fit confidence level cut of $1x10^{-4}$. It should be noted that the mean values and widths obtained from these Gaussian fits will serve as the observed massed and widths for the rest of this analysis. More specifically, the mass and width for the η was found to be $m_\eta = 0.545, \sigma_\eta = 0.02883$ (GeV/c^2); and the ϕ mass and width was found to be $m_\phi = 1.02, \sigma_\phi = 0.005917$ (GeV/c^2). Due to the high amount of statistics associated with this topology at this point, it was only necessary to include fifteen files to perform this study.

After the fits for the ϕ and η peaks were performed at different confidence levels, an integration of the Gaussian function and polynomial function was calculated. The results of these integrations plotted as a function of kinematic fit confidence level provides an indication of where an appropriate confidence level cut should be for this analysis. The outcomes of these integrations are provided in Figure 10 for the η meson and also in Figure 11 for the ϕ meson. Both figures contain a red and green line where the red line is the integrated value for the background polynomial and the green line is the integrated value for the Gaussian fit. Each plot contains ten points, denoted with a + symbol, which represent the values obtained at different kinematic fit confidence level values. One can easily observe that for both the ϕ and η plots, the integration of background events drops substantially as the kinematic fit confidence level cut becomes tighter. Additionally, the integration of signal events stays relatively flat as a function of cut value, an indication that the kinematic fitter is performing correctly. Ultimately, the value of $1x10^{-4}$ was chosen as the final kinematic fit cut value since it removed a large amount of background events for both the ϕ and η, while also preserving an appropriate amount of signal events.

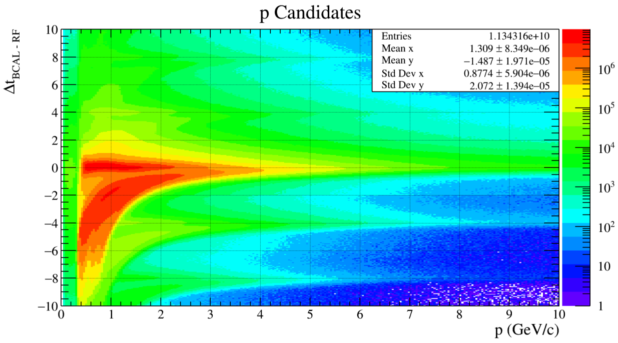

(a) Δ T Vs P for Proton candidates that have the Barrel Calorimeter as the timing detector.

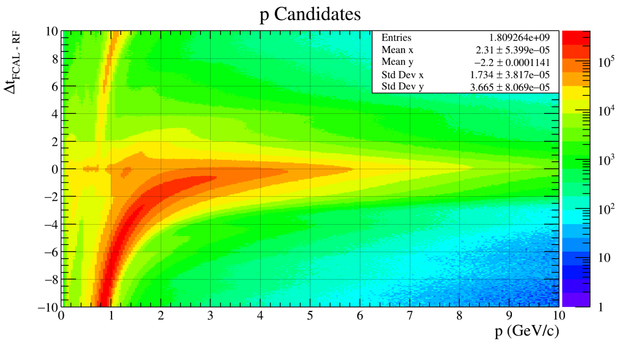

(b) Δ T Vs P for Proton candidates that have the Forward Calorimeter as the timing detector.

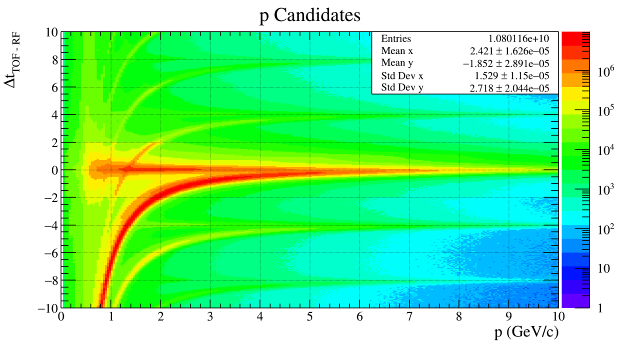

(c) Δ T Vs P for Proton candidates that have the Time of Flight as the timing detector.

Figure 1: Timing plots for proton candidates at GlueX. Protons are identified by selecting the horizontal band centered about $\Delta T = 0$. The curved line deviating below the horizontal proton line comes from miss identified π^+ tracks. The additional curved lines above and below $\Delta T = 0$ come from π^+ tracks that are associated with the wrong RF bunch.

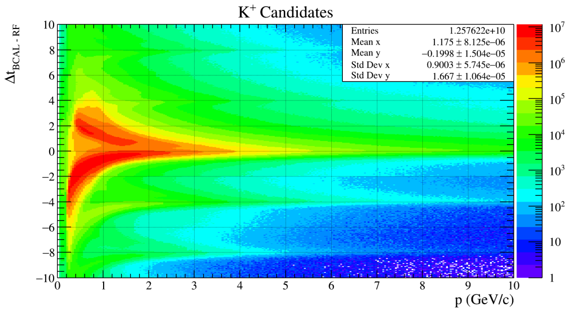

(a) Δ T Vs P for K^+ candidates that have the Barrel Calorimeter as the timing detector.

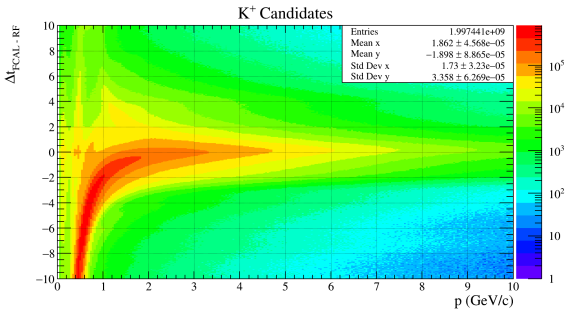

(b) Δ T Vs P for K^+ candidates that have the Forward Calorimeter as the timing detector.

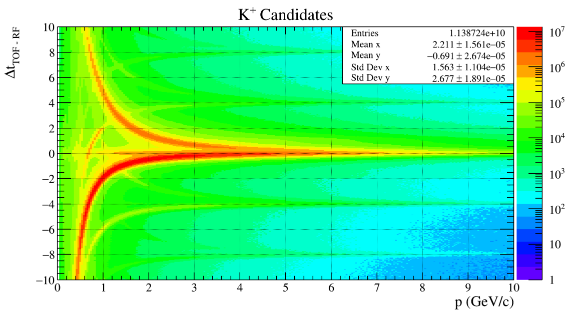

(c) Δ T Vs P for K^+ candidates that have the Time of Flight as the timing detector.

Figure 2: Timing plots for K^+ candidates at GlueX. K^+ are identified by selecting the horizontal band centered about $\Delta T = 0$. The curved line deviating below the horizontal K^+ line comes from miss identified π^+ tracks, and the curved line deviating above the horizontal K^+ line comes from miss identified proton tracks. The additional curved lines above and below $\Delta T = 0$ come from π^+ and proton tracks that are associated with the wrong RF bunch.

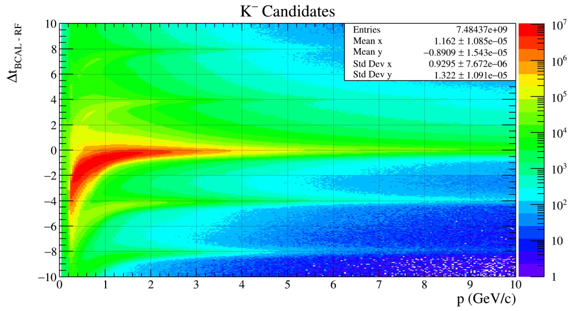

(a) Δ T Vs P for K^- candidates that have the Barrel Calorimeter as the timing detector.

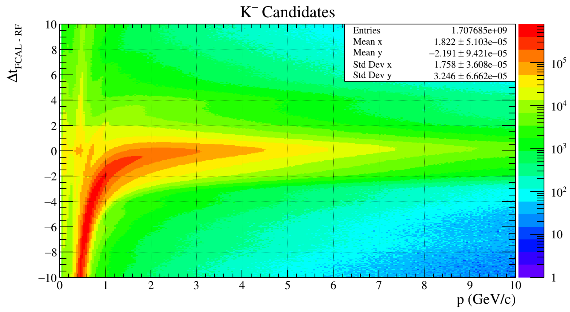

(b) Δ T Vs P for K^- candidates that have the Forward Calorimeter as the timing detector.

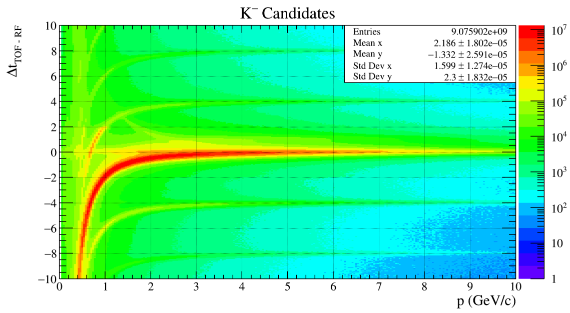

(c) Δ T Vs P for K^- candidates that have the Time of Flight as the timing detector.

Figure 3: Timing plots for K^- candidates at GlueX. K^- are identified by selecting the horizontal band centered about $\Delta T = 0$. The curved line deviating below the horizontal K^- line comes from miss identified π^- tracks. The additional curved lines above and below $\Delta T = 0$ come from π^- tracks that are associated with the wrong RF bunch.

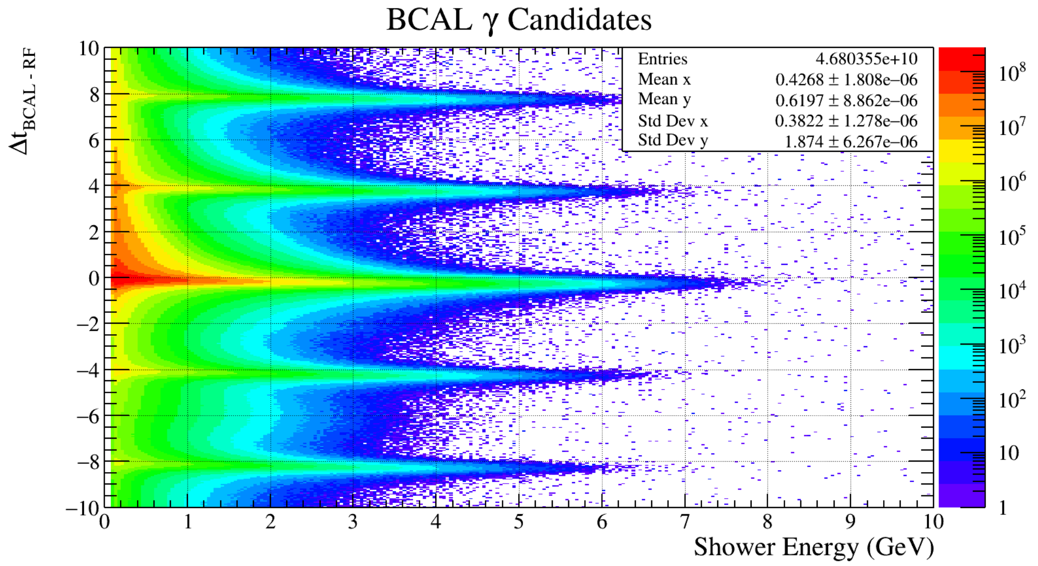

(a) Δ T Vs Shower Energy for γ candidates that have the Barrel Calorimeter as the timing detector.

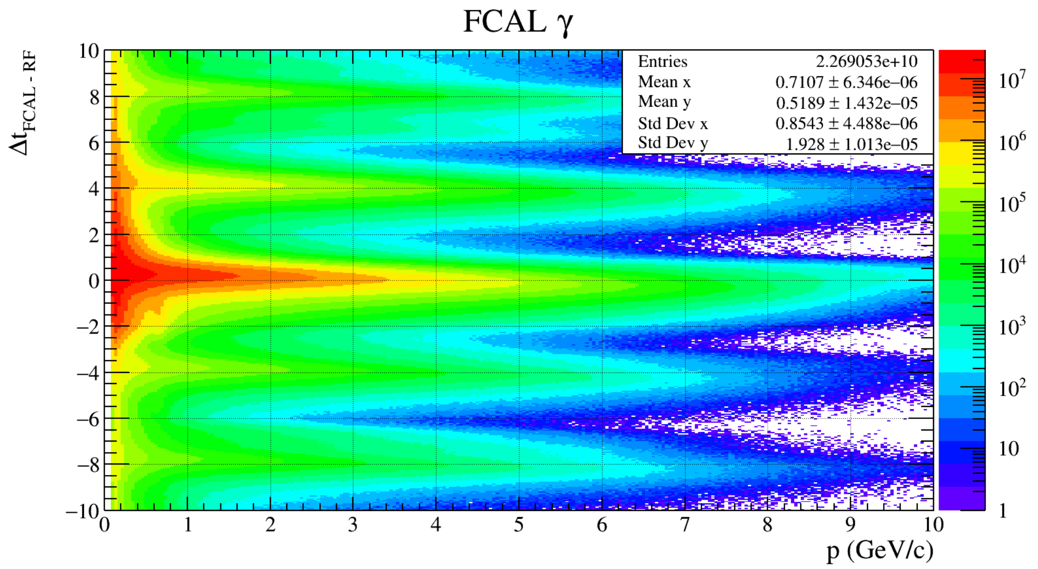

(b) Δ T Vs Shower Energy for γ candidates that have the Forward Calorimeter as the timing detector.

Figure 4: Timing plots for γ candidates at GlueX. γ are identified by selecting the horizontal band centered about $\Delta T = 0$. Large enhancement in statistics at low momentum and out of time with the γ line comes from slow moving and poorly times neutrons. The additional horizontal lines above and below $\Delta T = 0$ come from γ showers that are associated with the wrong RF bunch.

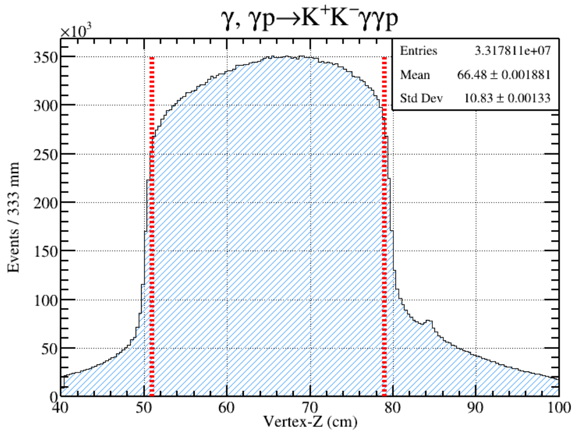

(a) Reconstructed vertex position along the beam direction for γ gamma candidates with cut lines at 51 and 79 cm.

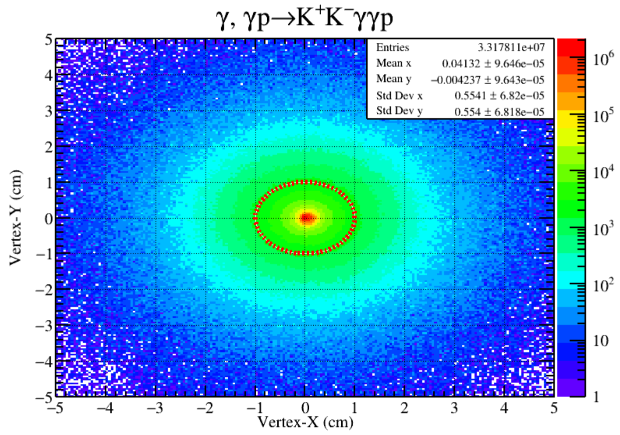

(b) Reconstructed vertex position transverse to the the beam direction for γ gamma candidates with cut a line at 1 cm in radial distance.

Figure 5: An example of what a reconstructed vertex distribution looks like for a final state γ in the reaction $\gamma p \to pK^+K^-\gamma_1\gamma_2$. The upper image is the reconstructed vertex position along the beam line, or z axis; and the lower image is the reconstructed vertex position in the directions transverse to the beam line. Both figures contain red dashed lines which represent the cut values for all reconstructed final state particles. In the z direction the cut values are $51cm \leq V_z \leq 79cm$, and in the transverse direction the cut values are $V_r \leq 1cm$. The z direction cut values are established from Log Entry 3456336 from a Spring 2017 empty target run. The transverse cuts are simply established by considering the geometric size of the target chamber.

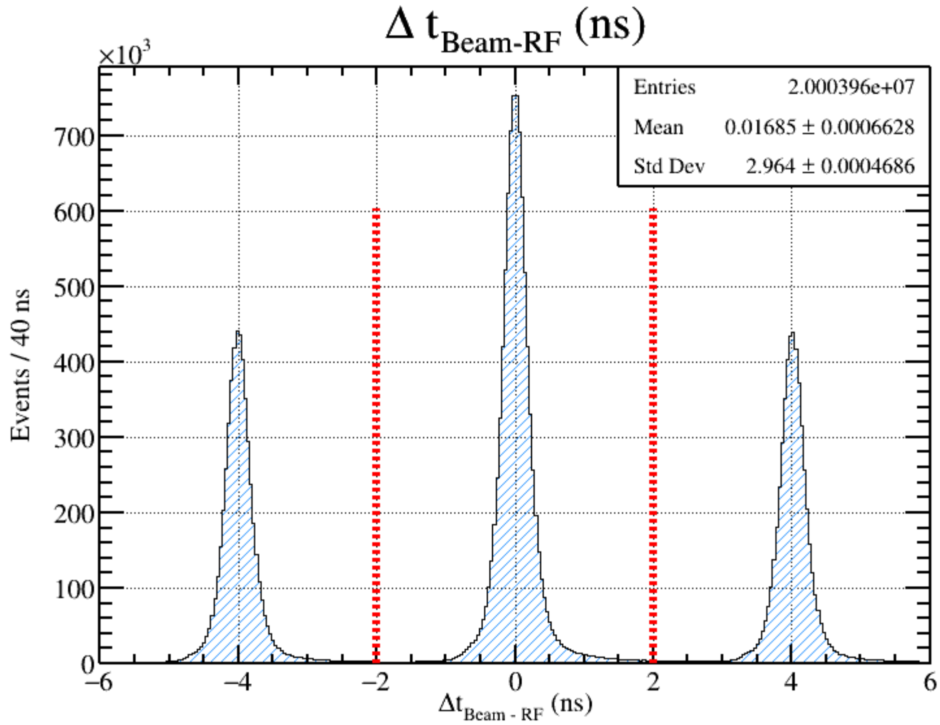

Figure 6: An example histogram of beam time as compared to the reported Radio Frequency (RF) time. In the plot there are three peaks, all of which are separated by four nanoseconds. Also included in the plot are two red dashed cut lines at ± 2 ns. These cut lines will select the beam time which agrees with the RF and will reject the other out of time beam particles.

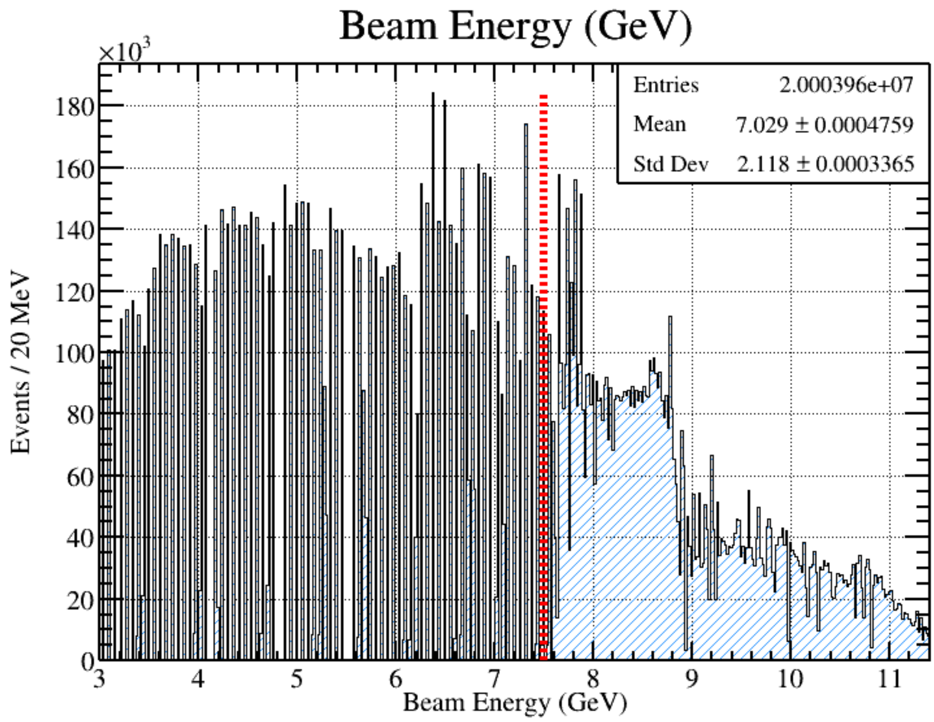

Figure 7: An example histogram of the beam energy distribution at GlueX. One can easily notice the large amount of statistics present around the coherent peak region ($8.0GeV - 8.8GeV$) and energies above it. Also contained in the image is a red dashed line which represents the cut value used on this data to select beam energies above 7.5 GeV.

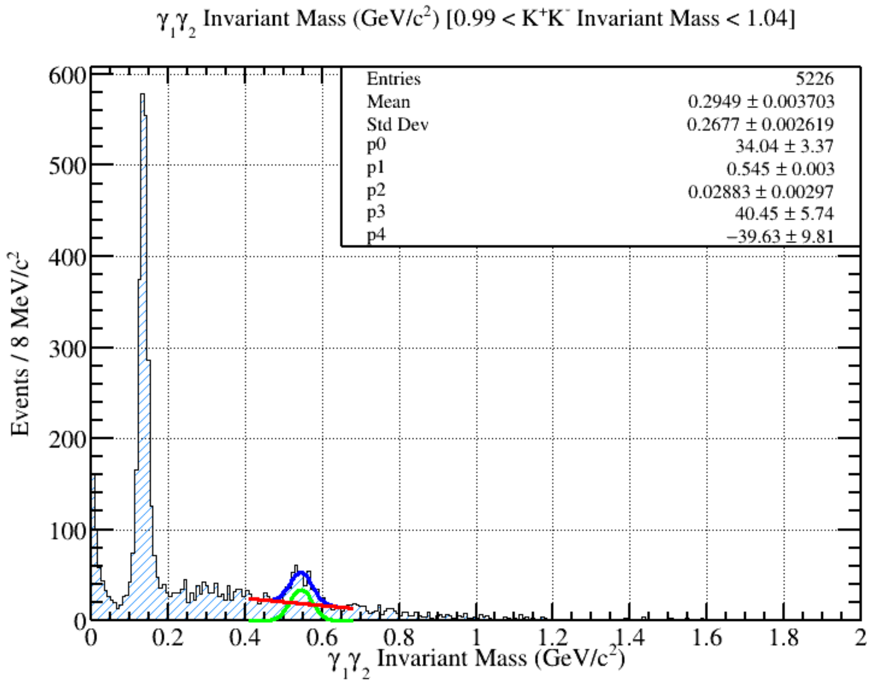

Figure 8: The $\gamma_1\gamma_2$ invariant mass obtained after a kinematic fit confidence level cut of $1x10^{-4}$ and requiring the K^+K^- invariant mass be between the values of 0.99 and 1.04 GeV/c^2 in order to reduce redundant backgrounds. The spectra shows clear π^0 and η peaks at appropriate mass value. The figure also includes three fits where the blue line represents a Gaussian plus a first degree polynomial, the green line represents the Gaussian fit, and the red line represents the first degree polynomial. The constants associated with these fits are listed in the legend.

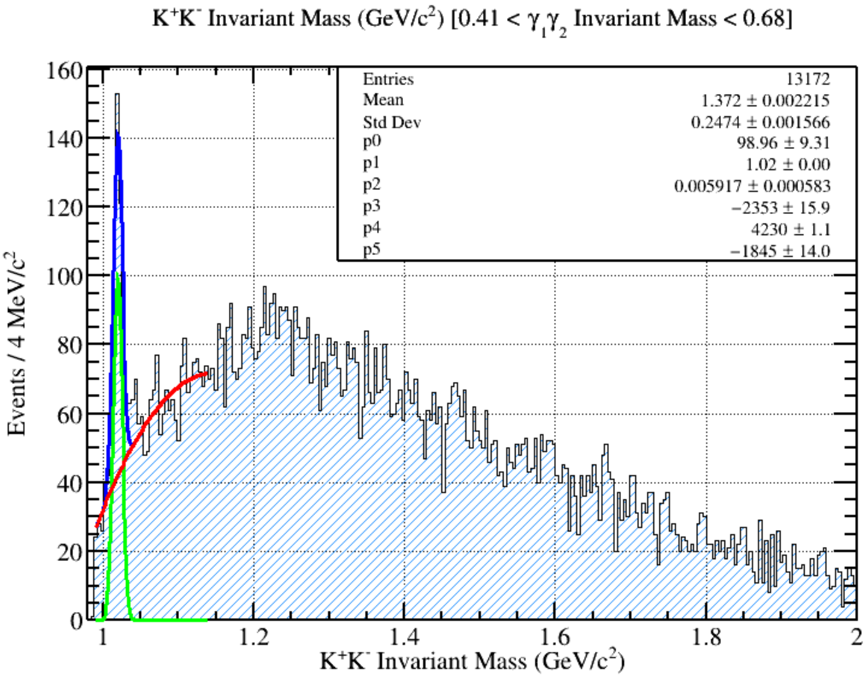

Figure 9: The K^+K^- invariant mass obtained after a kinematic fit confidence level cut of $1x10^{-4}$ and requiring the $\gamma_1\gamma_2$ invariant mass be between the values of 0.41 and 0.68 GeV/c^2 in order to reduce redundant backgrounds. The spectra shows a clear ϕ peak with a minimal amount of background. The figure also includes three fits where the blue line represents a Gaussian plus a second degree polynomial, the green line represents the Gaussian fit, and the red line represents the second degree polynomial. The constants associated with these fits are listed in the legend.

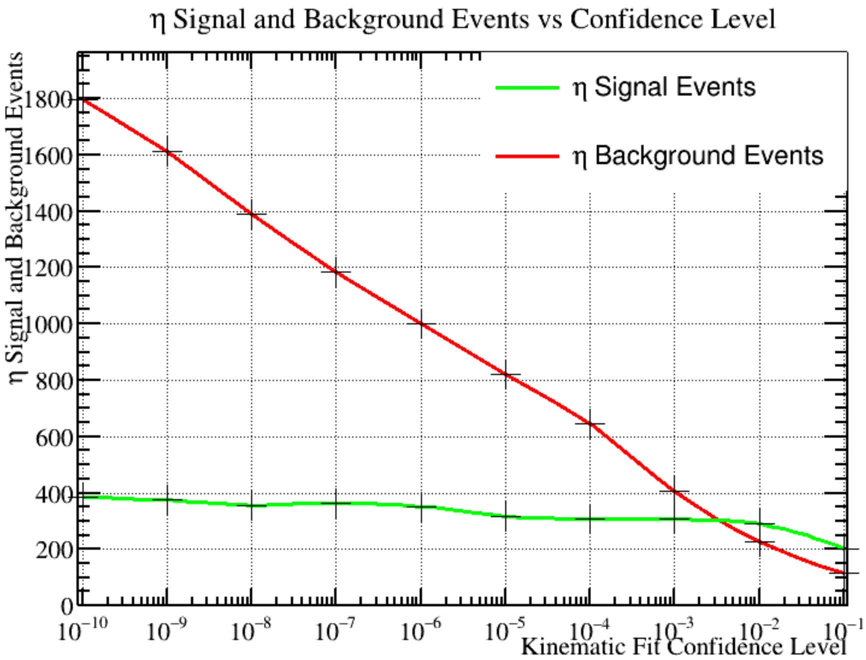

Figure 10: A graph of the η signal and background events as a function of the kinematic fit confidence level cut. The graph contains a red line which represents the integrated η background events from a first order polynomial, and a green line which represents the integrated η signal events from a Gaussian fit function. The graph indicates that the kinematic fitter is working appropriately such that the total number of background events falls as the kinematic fit confidence level cut is increased. Additionally, the total number of signal events stays relatively flat. This graph helps to provide an appropriate kinematic fit cut value that will be used for the rest of this analysis.

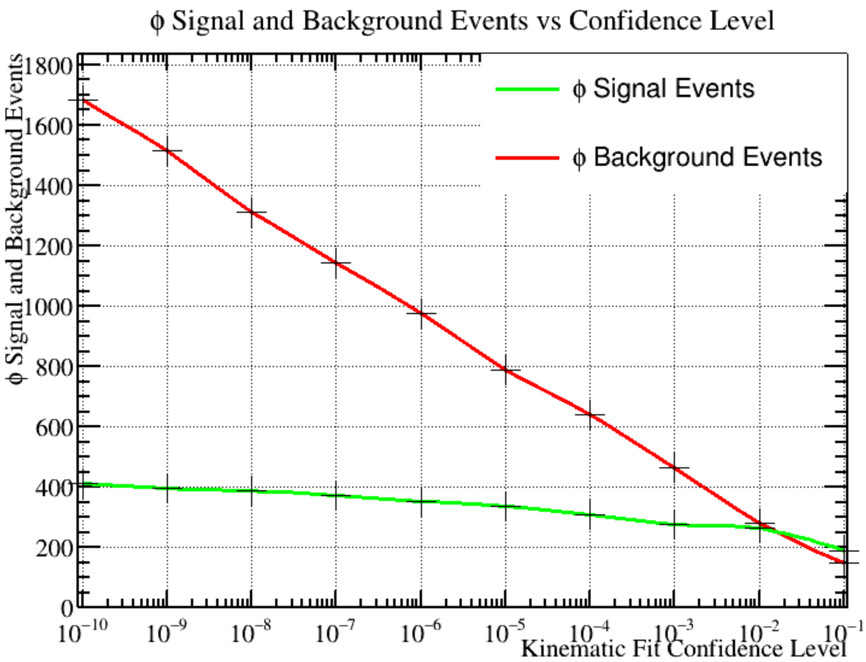

Figure 11: A graph of the ϕ signal and background events as a function of the kinematic fit confidence level cut. The graph contains a red line which represents the integrated ϕ background events from a second order polynomial, and a green line which represents the integrated ϕ signal events from a Gaussian fit function. Just like the η graph before it in Figure 8, the total number of background events falls as the kinematic fit confidence level cut is increased and the total number of signal events stays relatively flat.

2 Investigation of $\phi\eta$ correlation by means of K^+K^- Vs $\gamma_1\gamma_2$ Invariant Mass Plot

The image illustrated in Figure 12 is the data in question. On the vertical axis is the K^+K^- invariant mass and on the horizontal axis is the $\gamma_1\gamma_2$ invariant mass. To be absolutely clear, this is a plot of invariant mass versus invariant mass and is therefore not a Dalitz Plot. Some interesting features contained within the image are the clear vertical bands for the π^0 and η resonances which have large decay modes to $\gamma\gamma$ final states. In addition, one can also observe a horizontal band slightly above 1 $\frac{GeV}{c^2}$ which corresponds to the ϕ meson decaying to a K^+K^- final state. This analysis will focus on the region where the ϕ meson and η meson bands cross in order to determine if their intersection region contains some type of correlation.

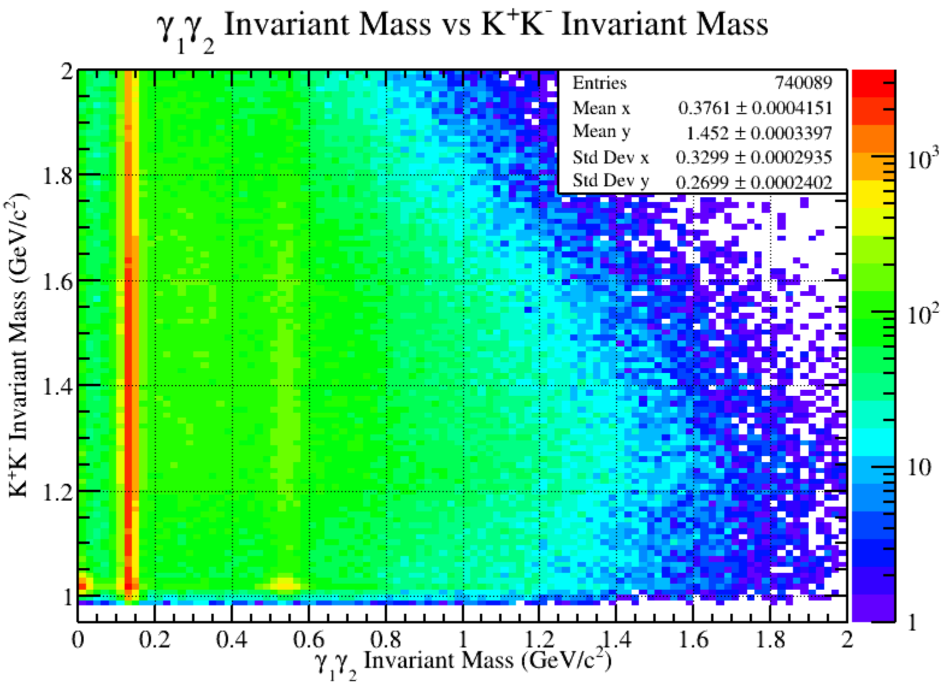

Figure 12: A two dimensional invariant mass plot with the K^+K^- invariant mass on the vertical axis, the $\gamma_1\gamma_2$ invariant mass on the horizontal axis, and a logarithmically scaled z axis. Some interesting features contained within the image are the clear vertical bands for the π^0 and η resonances which have large decay modes to $\gamma\gamma$ final states. In addition, one can also observe a horizontal band slightly above 1 $\frac{GeV}{c^2}$ which corresponds to the ϕ meson decaying to a K^+K^- final state.

2.1 Cuts on the 2D Invariant Mass Plot

In order to analyze the $\phi\eta$ region of this data, only events which fall within $\pm 10\sigma_\phi$ away from the ϕ peak and $\pm 10\sigma_\eta$ away from the η peak will be considered. This was done by taking different slices of either the $\gamma\gamma$ or K^+K^- data, then projecting the invariant mass distribution onto the opposite axis. For example, there were five different ϕ mass regions studied in this analysis. Each fit corresponds to a different $\gamma\gamma$ mass range. The $\gamma\gamma$ mass ranges are all $4\sigma_\eta$ in width, and span a total mass range of $m_\eta - 10\sigma$ to $m_\eta + 10\sigma$. An illustrated example with labeled cut lines is provided in Figure 13. It should be noted that the analysis of the η mass was not studied symmetrically about the ϕ due to the fact that going more than $m_\phi - 6\sigma_\phi$ away from the ϕ peak would result in no events because of the K^+K^- threshold.

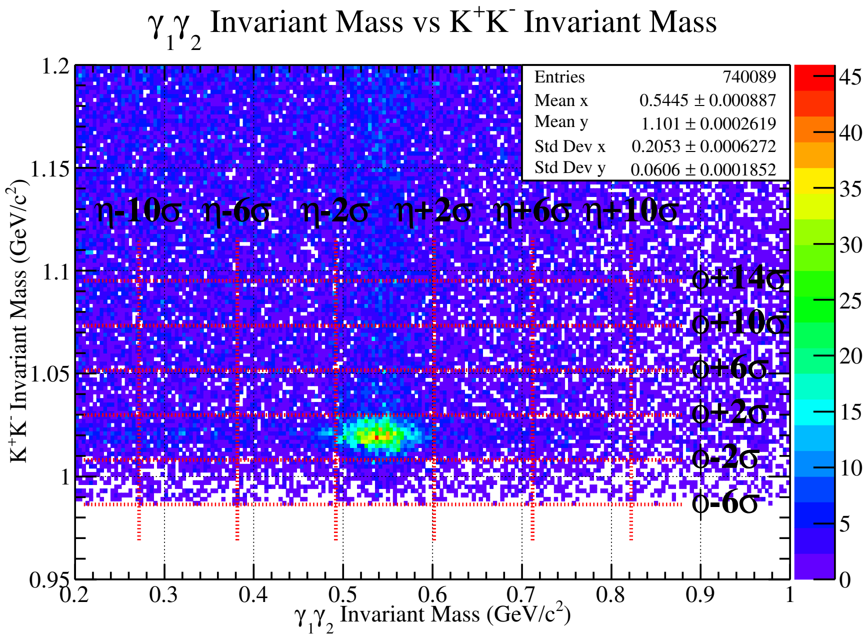

Figure 13: An illustrated example of the cuts used for studying the correlation of $\phi\eta$. The figure above is a two dimensional invariant mass plot which clearly shows an η band spanning the vertical direction at $\sim 0.547 GeV/c^2$ and a ϕ band spanning the horizontal direction at $\sim 1.02 GeV/c^2$. The red vertical and horizontal cut lines provide the ranges used to study $\phi\eta$ correlation. Examples of what the projected ranges look like are provided in Figures [14][15].

2.2 Projections and Fits for ϕ and η

Once the data had been cut and projected in the ten different mass regions, the ϕ and η peaks were fit. In the instance of the ϕ meson, the signal plus background events were fit with a Gaussian plus a second degree polynomial. The fit range used in each histogram projection for the ϕ meson spans from $m_\phi - 6\sigma_\phi$ to $m_\phi + 30\sigma_\phi \, \frac{GeV}{c^2}$. The unusually large fit range was necessary in order to properly estimate the background surrounding the ϕ mass. In the instance of the η meson, the signal plus background events were fit with a Gaussian plus a first degree polynomial due to the relatively flat background surrounding the η peak. The fit range used for the η meson spans $m_\eta \pm 6\sigma_\eta \, \frac{GeV}{c^2}$. The resulting fits are provided in the images below where the blue line represents the fit for all events (signal plus background), the green line represents the Gaussian fit (signal events), and the red line represents the polynomial fit (background events). Each histogram contains a title with brackets at the end. The arguments encapsulated by the brackets is the cut range that was used for that particular projection sample.

2.3 Integration Results for ϕ and η

After obtaining accurate fits for all regions, integration of the Gaussian fit functions was performed. Each Gaussian fit was integrated in the range of $m \pm 2\sigma_m$, where m represents either m_ϕ or m_η mass coupled with the addition or subtraction of two standard deviations in each direction. Integration of the Gaussian fits provides an accurate estimate for the number of signal events that exists for that particular sampling of $\gamma\gamma$ Vs K^+K^- phase space. The estimated number of signal events have been added to the 2D mass plot below, with the exception of the $\phi\eta$ intersection region which will be discussed in more detail in the Conclusion section.

2.4 Additional Statistics Study

In addition to the analysis mentioned above, an additional study has been included which simply samples the phase space and records the number of events within that sample. To do this, the same cut ranges as before were used. The only difference is that only the 3x3 grid surrounding the $\phi\eta$ intersection region. Each region is a box cut which is exactly $4\sigma_\phi$ x $4\sigma_\eta$ in area. Each area is given an index to denote the specific region of phase space that is being sampled and an illustration is provided below.

Using the diagram as a reference, it is easy to see that the average number of background events within this phase space can be calculated using the

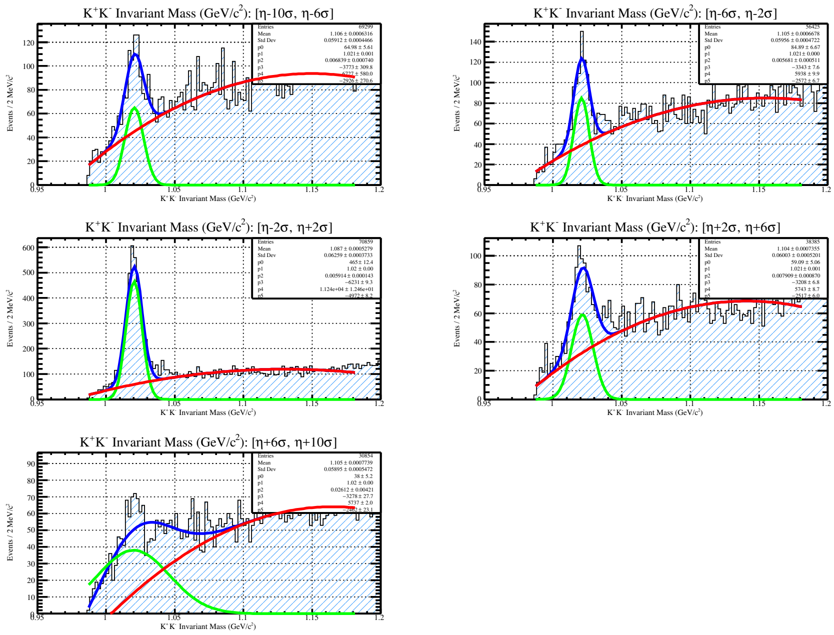

Figure 14: A collection of different K^+K^- Invariant Mass projections as a function of $\gamma_1\gamma_2$ Invariant Mass cut range. Each sub figure includes a red line which is a second degree polynomial used to estimate the shape of the background, a green line which is a Gaussian used to estimate the ϕ signal peak, and a blue line which the sum total of the polynomial fit and Gaussian fit. Lastly, each sub figure also includes the $\gamma_1\gamma_2$ Invariant Mass cut range used to produce the projected figure. This information is in the title of the histogram, inside the brackets.

formula $N_{BG} = (A_1 + A_3 + A_7 + A_9)/4$. Additionally, the average number of ϕ and η events plus background can be calculated using $N_{BG} + N_\phi = (A_4 + A_6)/2$ and $N_{BG} + N_\eta = (A_2 + A_8)/2$, respectively. Lastly, quantification of the number of correlated events in region 5 is possible by using $N_{BG} + N_\phi + N_\eta + N_{correlated} = A_5$. A figure with the number of events contained within each region of phase space is given below.

The first step of this simplistic analysis is to determine what the average number of background events is, which is calculated to be 453. Knowing this, the number of ϕ and η events can now be determined by using the equations $N_{BG} + N_\phi = (A_4 + A_6)/2$ and $N_{BG} + N_\eta = (A_2 + A_8)/2$, and then subtracting the average number of background events. Upon doing

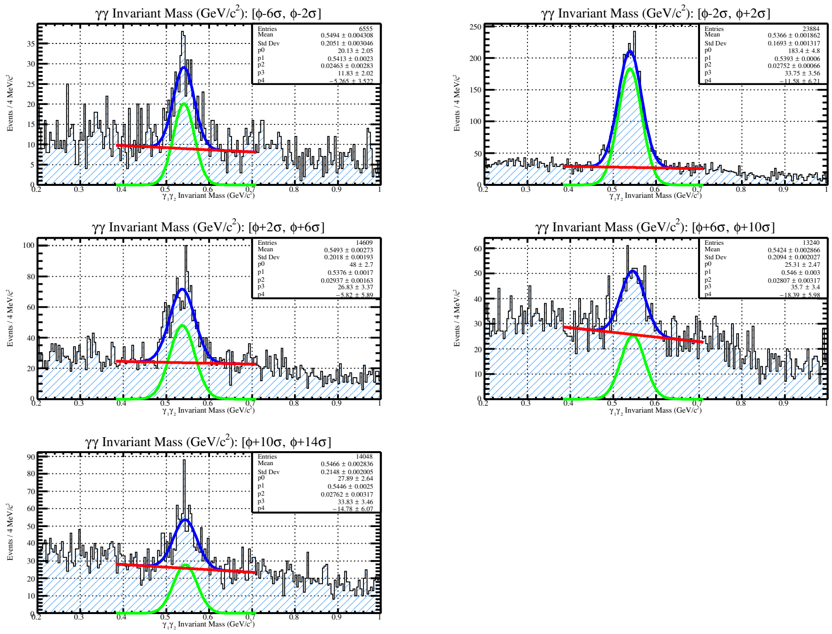

Figure 15: A collection of different $\gamma_1\gamma_2$ Invariant Mass projections as a function of K^+K^- Invariant Mass cut range. Each sub figure includes a red line which is a first degree polynomial used to estimate the shape of the background, a green line which is a Gaussian used to estimate the η signal peak, and a blue line which the sum total of the polynomial fit and Gaussian fit. Lastly, each sub figure also includes the K^+K^- Invariant Mass cut range used to produce the projected figure. This information is in the title of the histogram, inside the brackets.

this, it was fount that N_ϕ is 423 and N_η is 433. To complete this analysis, the number of correlated events can now be estimated by using the equation $N_{BG}+N_\phi+N_\eta+N_{correlated} = A_5$, and subtracting N_{BG}, N_ϕ, and N_η. The total number of correlated events is 2446. This calculations shows once again that there is an overflow of events within the $\phi\eta$ intersection region that cannot be explained by the presence of background or the addition of events from the ϕ and η bands.

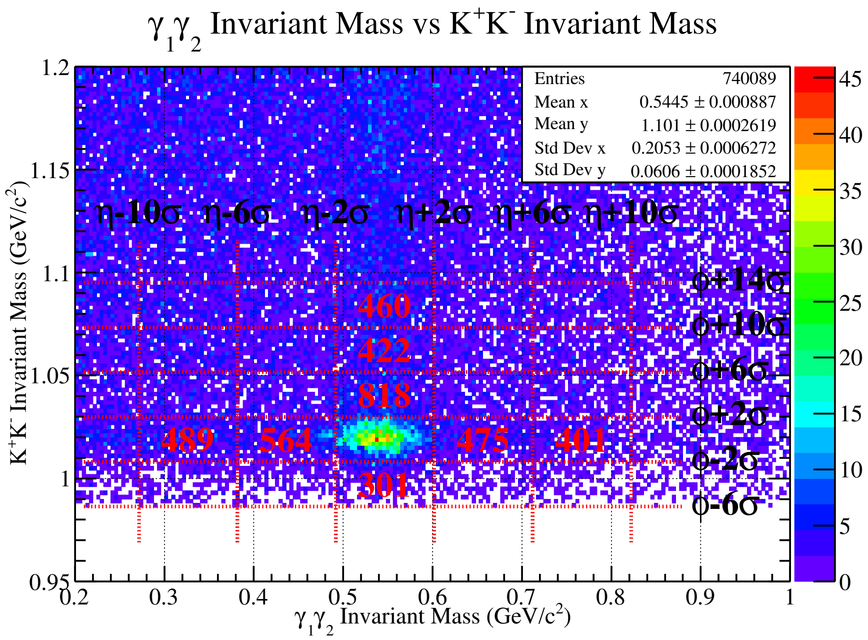

Figure 16: The above figure provides the number of events for each projection range studied. These numbers were calculated by means of integrating the Gaussian fit for either the ϕ or η between $\pm 2\sigma$. The vertical column of numbers represents the number of η events for a given K^+K^- Invariant Mass, and the horizontal row of numbers represents the number of ϕ events for a given $\gamma_1\gamma_2$ Invariant Mass. The number of events observed in the intersection region was not included in the figure due to the amount of space available. There numbers can be found in the Conclusion section.

2.5 Conclusion of K^+K^- Vs $\gamma_1\gamma_2$ Invariant Mass Plot Study

Given that the number of estimated signal events has been calculated for the ϕ and η bands which neighbor the $\phi\eta$ intersection region, the expected number of events will be in the $\phi\eta$ intersection region using averages can be estimated. Taking the numbers from the two dimensional plot above and rounding to the nearest integer, the average number of signal events in the ϕ band is $\overline{\phi_{events}} \sim 482$, and the average number of signal events in the η band is $\overline{\eta_{events}} \sim 500$. Therefore, it is estimated that the number of signal events within the $\phi\eta$ intersection region should be just shy of 1000 events if

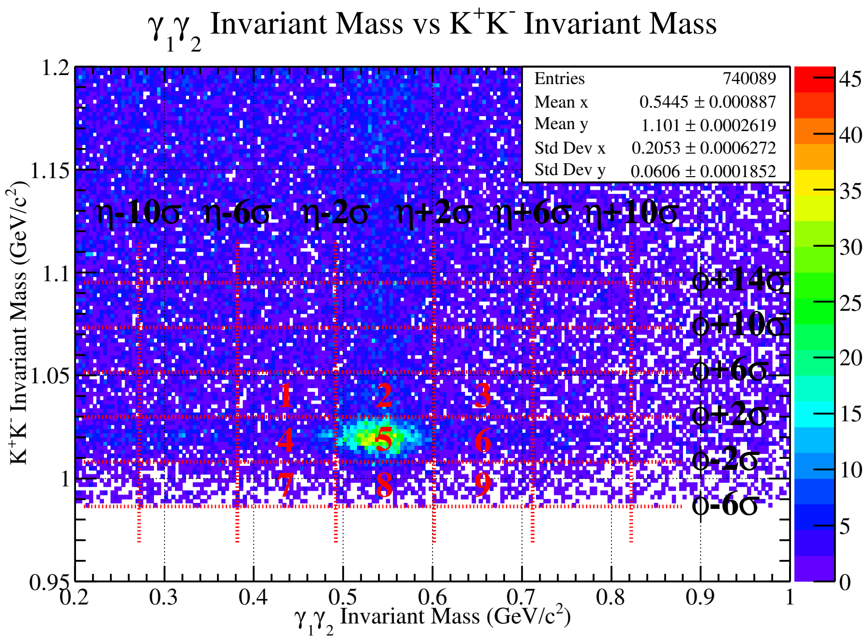

Figure 17: An illustration to provide the reader with an idea of how the second statistics study is performed. All of the cut ranges are identical to the first statistics study. The numbers provided in the figure do not represent events, but simply indicate the index associated with a certain area of $\phi\eta$ phase space.

there is no correlation present. After integrating the Gaussian fit for the ϕ and η mesons in the $\phi\eta$ intersection region, it was found that there were 3194 events corresponding to the ϕ fit, and 2993 events corresponding to the η fit. Both of these fits not only yield roughly the same number of events, but they also produce an event estimate which is a factor of three higher than what would have been there from the ϕ and η bands alone. The large increase in event statistics within the $\phi\eta$ intersection region strongly suggests that some type of correlation is present within this area of K^+K^- $\gamma\gamma$ phase space. It should be clearly noted that the nature of this correlation is not identified at this time. Moreover, it is unclear from this study as to whether or not the bound stats is mesonic or baryonic in nature. Additional studies on this area of phase space need to be performed in order to establish that this spike in statistics is not coming from the $\gamma p \to N^*\phi$, $N^* \to p\eta$ topology.

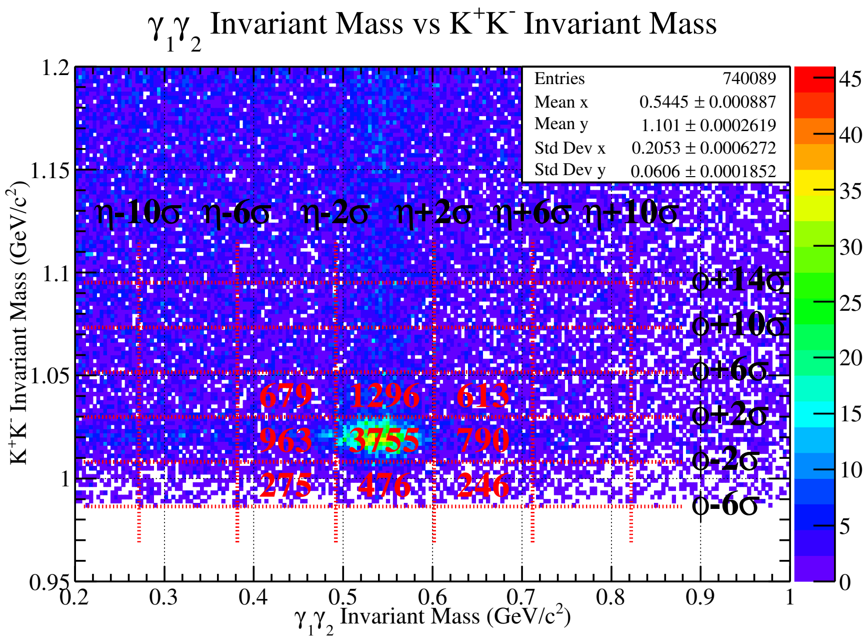

Figure 18: This figure shows the total number of counts in each box. To b be clear, the numbers in each are do not represent the total number of events, but rather the precise amount of statistics contained. Upon inspection, one can see evidence of $\phi\eta$ correlation, which is explained in the Conclusion section.

3 Monte Carlo

3.1 Monte Carlo Features of $\gamma p \to p\phi\eta$

In order to better understand the acceptance of the $\gamma p \to p\phi\eta$ topology in the GlueX spectrometer, a generated Monte Carlo sample was analyzed. More specifically, the exact sample that was produced was $\gamma p \to pX; X \to \phi\eta; \phi \to K^+K^-; \eta \to \gamma\gamma$. This Monte Carlo sample consisted of 170 k generated events for each of the run numbers 030408, 030620, 030802, and 031029. There run numbers were chosen because the first two have beam polarizations in the PARA/PERP directions at low intensity, and the second two have PARA/PERP orientations at high intensity. The total number of generated $\phi\eta$ events is therefore 680 k. The events were generated using a coherent bremsstrahlung beam energy spectrum and a t-slope of 4 $(GeV/c^2)^2$. To be more clear, the thrown beam particles were not polarized in this sample;

only the beam energy spectrum matched that of a polarized beam spectrum (Figure [19]). All final state particle kinematics were generated using the ROOT object TGenPhaseSpace. The generated final state phase space was flat and therefore did not include any spin information from parent or daughter states. The $\gamma, K^+, K^-, \phi, \eta$, and p particles were generated using the invariant mass values provided in the PDG. The photoproduced X mass was randomly distributed between the lower kinematic limit $m_\phi + m_\eta$ and the upper kinematic limit which is a function of the thrown beam energy.

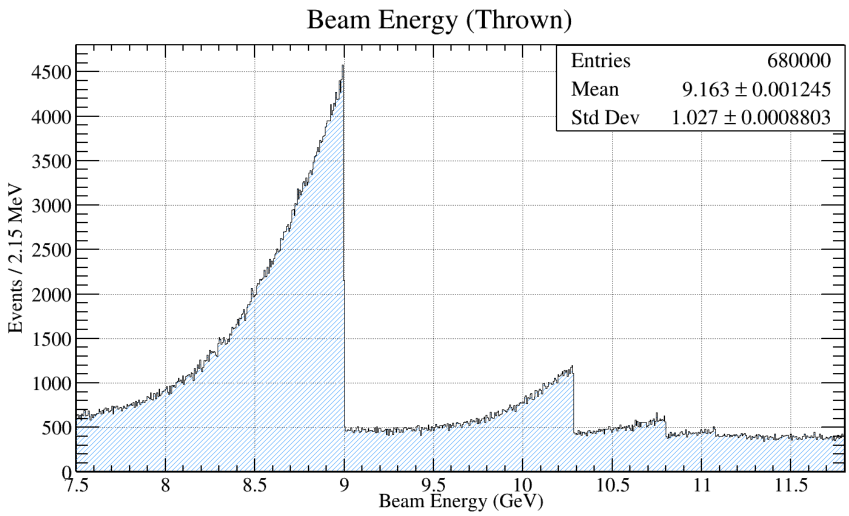

Figure 19: A histogram which includes the thrown beam statistics from the generated Monte Carlo example. In the figure one can easily see the coherent peak which maximizes at 9 GeV. Additionally, one can also see other secondary peaks at higher energy.

An example of what the generated beam energy distribution looks like for this Monte Carlo sample is given in Figure [19]. It should be noted that this particular Monte Carlo sample only generated beam energies between the values of $7.5 - 11.8$ GeV. The reason for the lower energy boundary of the beam energy spectrum is to both cut out potential areas of background due to low energy beam photons and to allow a larger sampling of polarized photons when a beam asymmetry study is performed with actual data. The high energy cut off of 11.8 GeV is simply there to match the high energy cut off of the Spring 2017 run.

Momentum versus theta distributions are also provided in Figures [20], [21], [22], and [23]. These figures are not accepted Monte Carlo, they are only the generates four vectors of the final state particles before running hdgeant, mcsmear, or `hd_root`. Still, the figures provide some insight into the expected

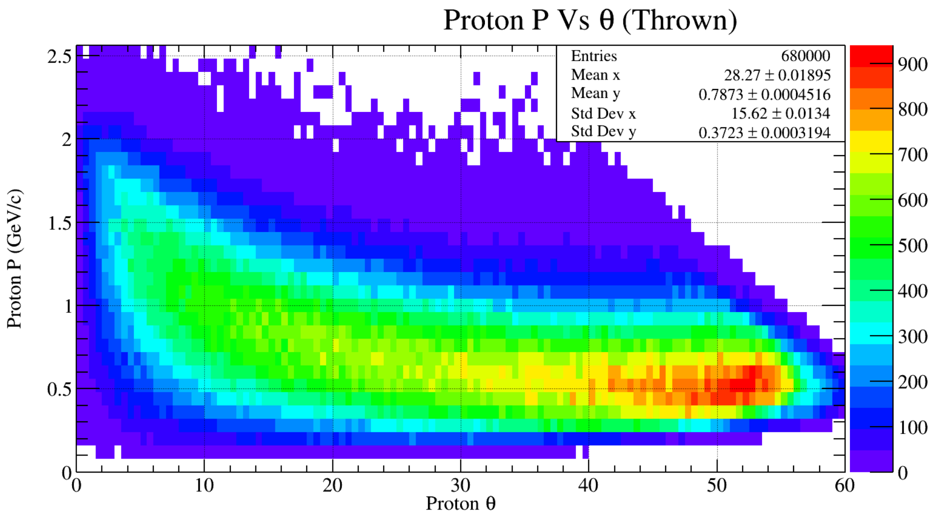

Figure 20: A two dimensional histogram which includes the thrown kinematic information of the recoil proton. In the histogram, the horizontal axis represents the generated θ angle in the lab frame, and the vertical axis represents the generated momentum magnitude in the lab frame. One interesting feature of this Monte Carlo data is that the protons kinematics appear to be constrained between $[0.2 - 2.0] GeV/c$ in momentum, and $[0.0 - 60.0]$ in angle.

kinematic distributions of the final state particles. For example, Figure [20] displays the momentum versus theta distribution for the recoil proton. This figure shows that we should expect the proton to have a very low momentum and high recoil angle relative to the beam direction for this final state.

Additionally. Figures [21][22] show the same plot but for K^+ and K^-, respectively. In these figures, it is clear that Kaons will preferentially travel towards the TOF/FCAL and with a momentum that should include a lot of pion contamination (see Figures [39][46] for more information on pion contamination at high momentum).

Lastly, Figure [23] shows that the final state photons will be mostly forward going and therefore we should expect to see the majority of them interacting with the FCAL rather than the BCAL. It comes as no surprise that the Monte Carlo has generated photons and kaons that favor the forward direction, while the recoil proton has low momentum and a highly transverse direction. This is simply a consequence of the fact that a 'low t' interaction was programmed into the Monte Carlo, resulting in Figure [24].

The last few figures I wish to discuss in this section involve the study of invariant mass spectra. The first of which is the invariant mass of $\phi\eta$

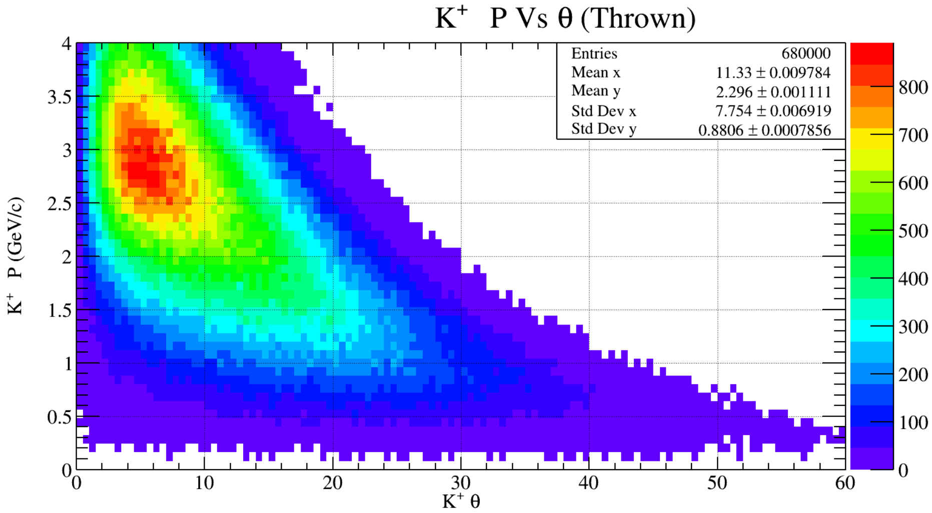

Figure 21: A two dimensional histogram which includes the thrown kinematic information of the generated K^+. In the histogram, the horizontal axis represents the generated θ angle in the lab frame, and the vertical axis represents the generated momentum magnitude in the lab frame.

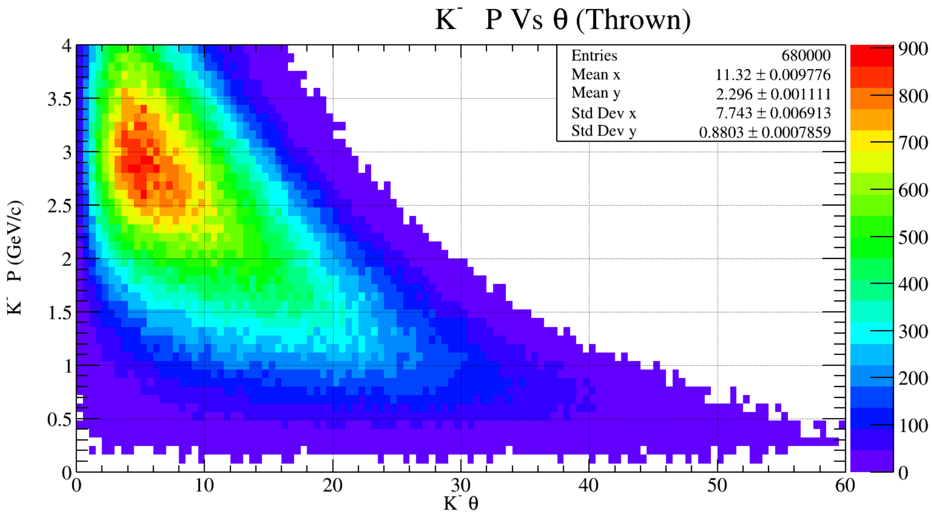

Figure 22: A two dimensional histogram which includes the thrown kinematic information of the generated K^-. In the histogram, the horizontal axis represents the generated θ angle in the lab frame, and the vertical axis represents the generated momentum magnitude in the lab frame.

(Figure [25]) which shows a flat distribution between the values of 1.5 to

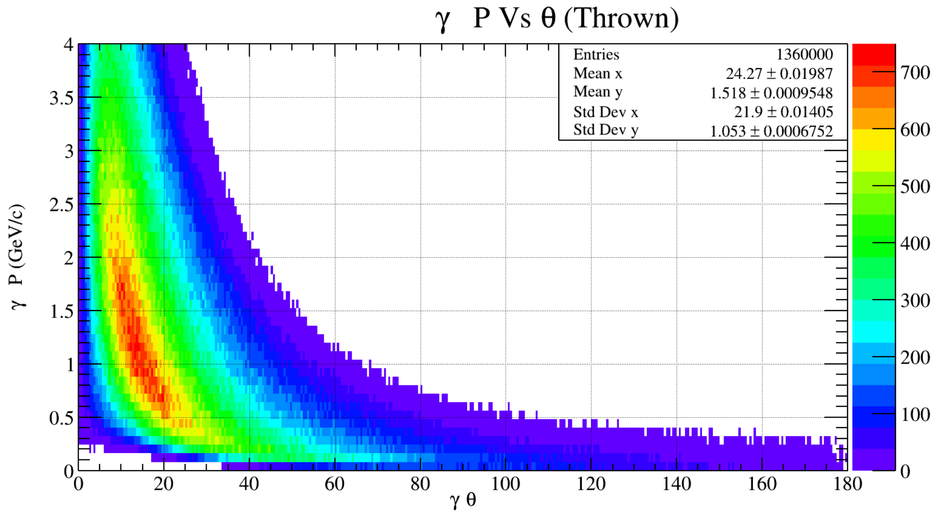

Figure 23: A two dimensional histogram which includes the thrown kinematic information of the generated photons. In the histogram, the horizontal axis represents the generated θ angle in the lab frame, and the vertical axis represents the generated momentum magnitude in the lab frame.

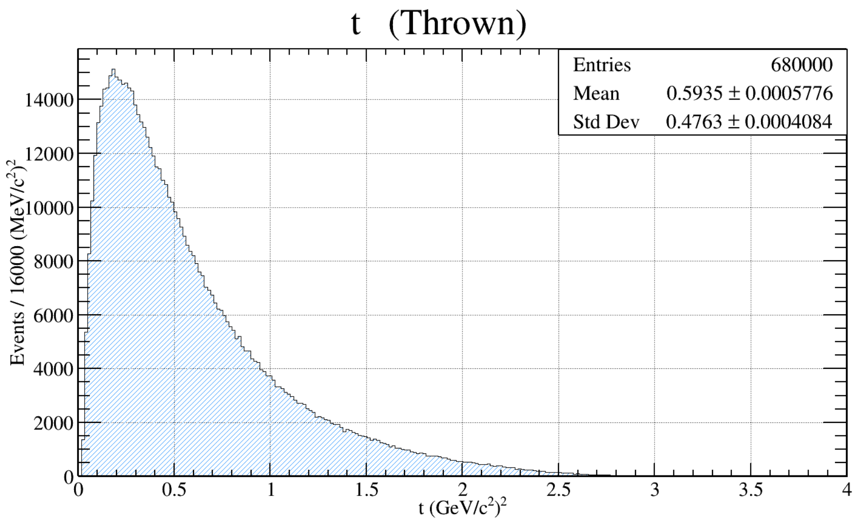

Figure 24: A histogram which includes the generated spectrum for the Mandelstam variable, t. The most important feature in this histogram is the fact that the majority of generated events come from low momentum transfer.

3 GeV/c^2; then the distribution drops off drastically until 3.3 GeV/c^2; and then less drastically from 3.3 to 4 GeV/c^2. These features may seem incor-

rect at first glance since the generated Monte Carlo mass is supposed to be flat. However, upon further inspection, it is clear that these features manifest themselves within the Monte Carlo data because of the shape of the beam spectra. The best way to see this behaviour is by considering Figure [26]. This figure shows the generated mandelstam variable t on the vertical axis, and the generated $\phi\eta$ mass on the horizontal axis. Since t is the momentum transfer, it is directly correlated with the beam photon and therefore will exhibit some coherent bremsstrahlung structure. This structure can be seen in Figure [26] where there is clear evidence of the beam energy spectra influencing the behavior of the $\phi\eta$ mass. We know from Figure [19] that the most dominant statistics will come from the coherent edge at 9 GeV and should drop off drastically beyond that point. This feature of the data is clearly seen in Figure [26] and is therefore the reason for the odd behavior seen in Figure [25].

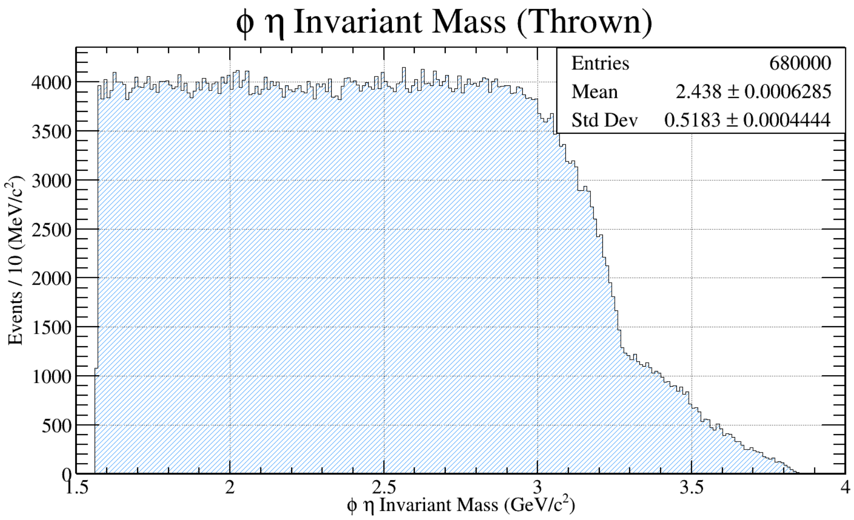

Figure 25: A histogram which includes the generated $\phi\eta$ invariant mass. In the figure one can easily see that the invariant mass of the $\phi\eta$ remains flat until it reaches $\sim 3.0GeV/c^2$. From that point, the invariant mass falls sharply until $\sim 3.3GeV/c^2$; and then continues to fall at a slower rate. This feature of the invariant mass is directly related to the fact that a coherent bremsstrahlung beam energy spectrum was used. The drastic drop off in statistics in the mass range of $3.0 - 3.3GeV/c^2$ is caused by the primary coherent peak at $9.0GeV$. To visualize this more clearly, see Figure [26].

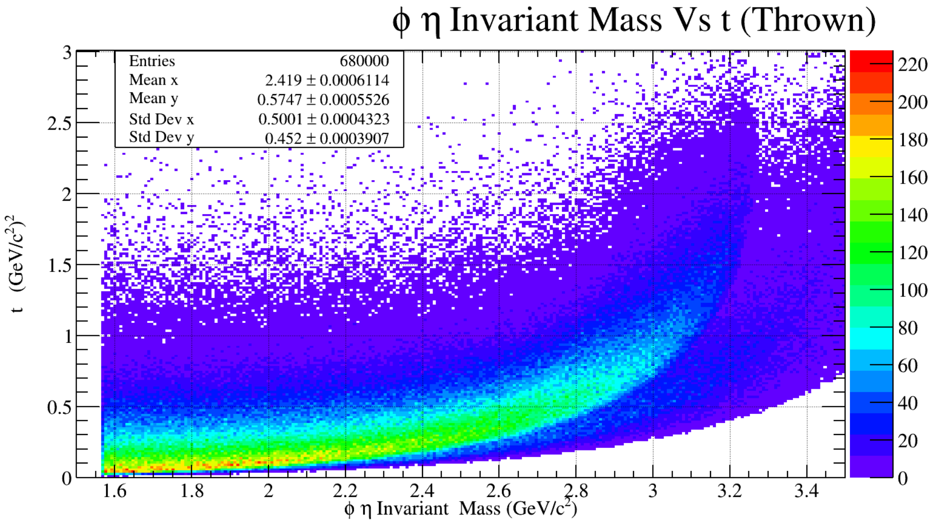

Figure 26: A two dimensional histogram which includes the generated $\phi\eta$ invariant mass on the horizontal axis and the Mandelstam t variable on the vertical axis. In the figure one can easily see the effect that the coherent peak has on the shape of the phase space. The effect can be seen in even greater detail in Figure [25].

3.2 A Monte Carlo Study to Determine ΔT Cuts

The timing cut values listed in Table [1] were determined by performing a full reconstruction of the Monte Carlo data discussed in the previous section. The procedure for reconstructing the Monte Carlo data is well known. First the four vectors of the $\gamma p \rightarrow pX; X \rightarrow \phi\eta; \phi \rightarrow K^+K^-; \eta \rightarrow \gamma\gamma$ topology are generated using TGenPhaseSpace. Next, the four vectors are fed into hdgeant where interactions with the detector are considered and all detector hits are interpreted using the geometry. After hdgeant completes, the Monte Carlo is then passed into mcsmear; which is responsible for taking the 'perfect' data from hdgeant and changing it to match the resolution of GlueX sub detectors. Upon mcsmear completion, the Monte Carlo procedure enters its final stage of reconstruction. This is done by calling the `hd_root` command coupled with a few plugins including `dana_rest`.

3.3 Evidence of Secondary Photons

Before performing this Monte Carlo study, it was well known that there was a lot of photon background seen in the data. After studying the data for quite some time, it was found that a two photon cut would destroy most

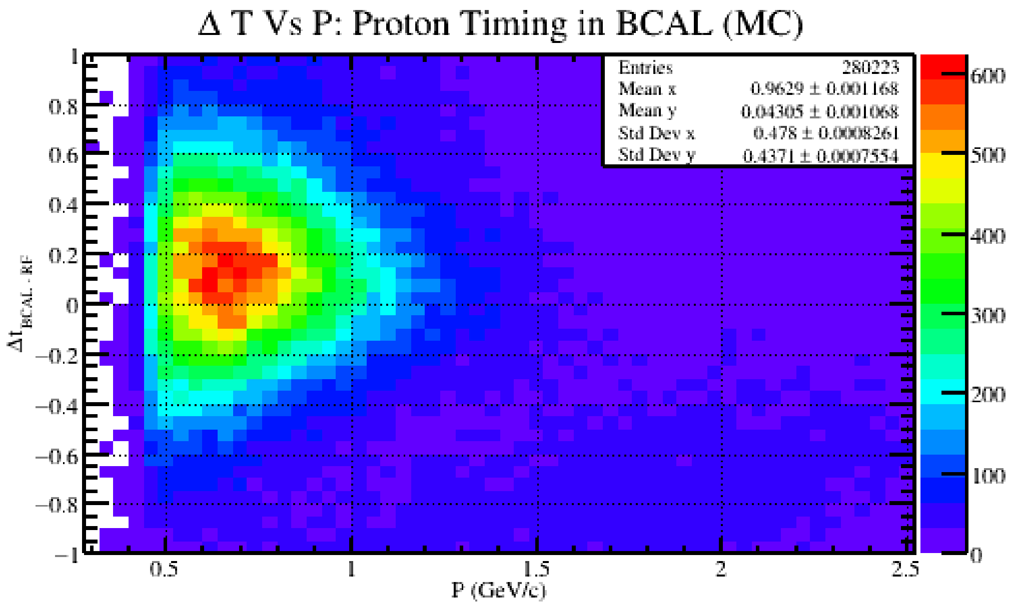

Figure 27: A timing plot for generated protons after reconstruction. The horizontal axis is the reconstructed momentum of the proton and the vertical axis is the timing difference between the BCAL and RF. The enhancement of statistics in the lower right portion of the plot comes from miss identified kaons that were also included in the Monte Carlo.

of the background associated with photons and would also result in an observed η resonance in a $\gamma\gamma$ invariant mass plot. At the time, it was unknown why the cut appeared to throw out a lot of photon background while simultaneously appearing to enhance signal. After carefully studying accepted Monte Carlo, background generated Monte Carlo (`bggen`), and data, it was found that much of this background is attributed to secondary photons. A secondary photon should be thought of as a photon that did not originate from any photoproduction reaction, nor from any expected decay of parent states. Therefore, a secondary photon can be thought of as a photon that arose from an interaction within the GlueX spectrometer from a final state particle. An example of a secondary photon that would be present in $\gamma p \to p\phi\eta$ data can be explained by means of high momentum and forward going kaons (Figures [21][22]). Since it is very likely that most of the kaons in this channel will interact with either the Time of Flight detector or the Forward Calorimeter, it is expected that these particle will deposit a lot of energy in this region of the spectrometer. These high momentum particles will cause a signal in one or both of these detectors and will also cause a

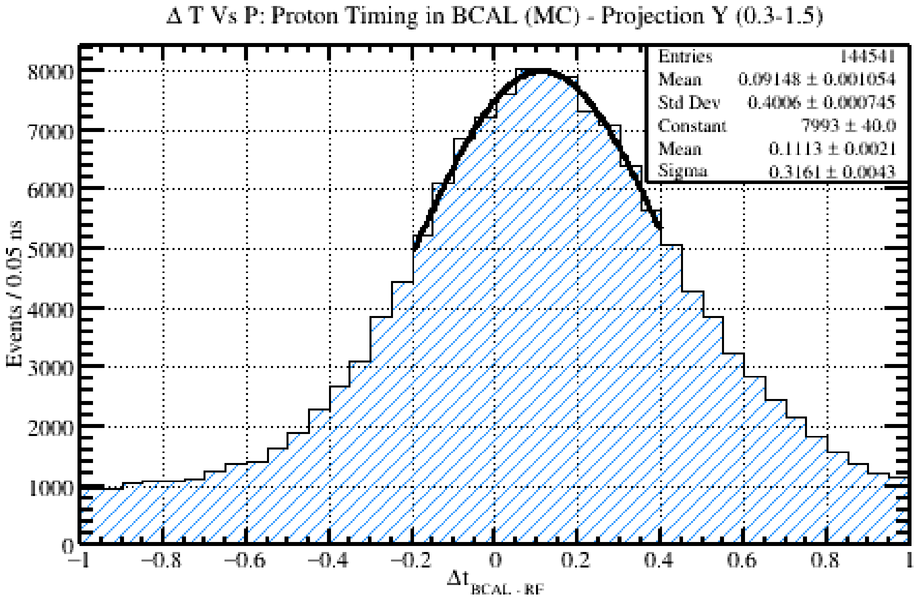

Figure 28: A projection of the statistics from Figure [27] onto the vertical (timing) axis between the momentum range of 0.3-1.5 GeV/C. This projection range was chosen so that the distortion from the lower kaon band was minimized. A Gaussian fit was performed and is included in the figure where the mean and width of the distribution are given in the legend.

'splash' effect near the signal region. This splash effect can cause some of the blocks in the Forward Calorimeter to absorb the extra energy and therefore become reconstructed photons in the data. The additional reconstructed photons will therefore cause the number of photons reconstructed in an event to be fictitiously higher than what was actually present within the detector. To first order, this perhaps explains why doing a two photon cut on data will both greatly reduce background and enhance a signal. However, many important questions will still remain about this cut. How much signal do we lose by simply performing a two photon cut? Furthermore, is there a better way to cut out the background and preserve as many signal events as possible? This subsection will show that this effect does in fact manifest itself in both Monte Carlo and data; and will perform an analysis on Monte Carlo and data to show the best way of reducing secondary photons.

The first evidence that suggests the existence of secondary photons in $\gamma p \to p\phi\eta; \phi \to K^+K^-; \eta \to \gamma\gamma$ accepted Monte Carlo can be seen by simply plotting the invariant mass of a reconstructed $\gamma\gamma$ pair (Figure [51]). The data which went into this plot was created by throwing $\gamma p \to p\phi\eta; \phi \to$

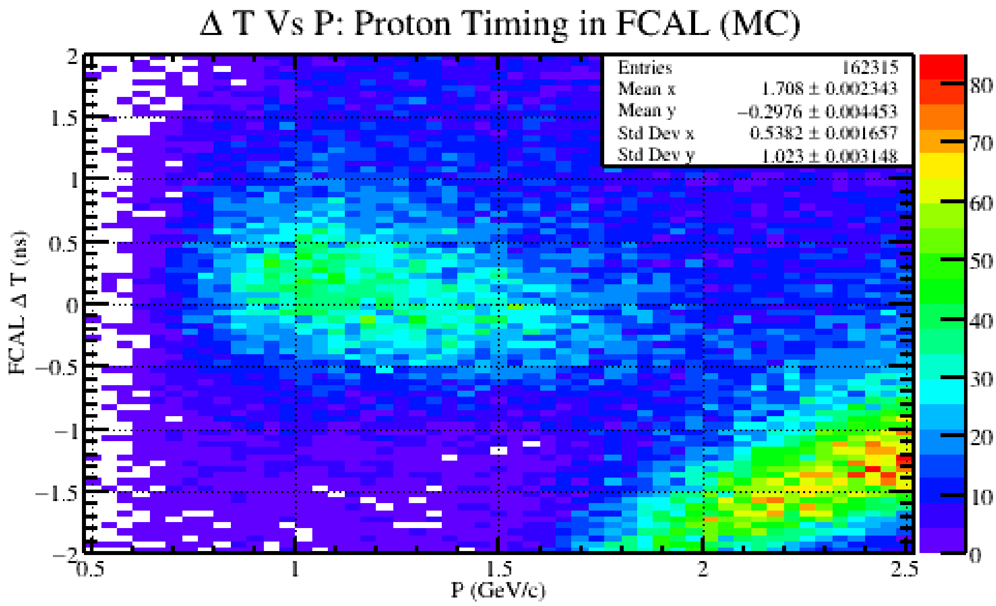

Figure 29: A timing plot for generated protons after reconstruction. The horizontal axis is the reconstructed momentum of the proton and the vertical axis is the timing difference between the FCAL and RF. The enhancement of statistics in the lower right portion of the plot comes from miss identified kaons that were also included in the Monte Carlo.

$K^+K^-; \eta \to \gamma\gamma$ into the GlueX detector and then simulating its behavior with `hdgeant` and `mcsmear`. The invariant mass spectrum in Figure [51] shows a clear peak from the generated η meson on top of a background that spans to low mass. If this sample initially only threw two photons exactly equal to the η meson invariant mass, then why are there so many low mass photon combinations that appear to be in the shape of background? To answer this question, we can separate our reconstructed Monte Carlo particles into two categories: particles that were generated and particles that were not generated. In doing so, we can see where this background comes from and also how to possibly reduce it.

We will first describe the background seen in Figure [51] by displaying P Vs θ and ϕ Vs θ plots for the thrown photons and the secondary photons in Figure [52]. The most important feature to take away from these plots is the tendency for secondary photons to be at a shallow angle relative to the beam direction (below 12°) while also having a low three momentum magnitude (below 500 MeV/c). Simply knowing the distribution of these photons gives us some insight into where they came from. Since neutral photons can only

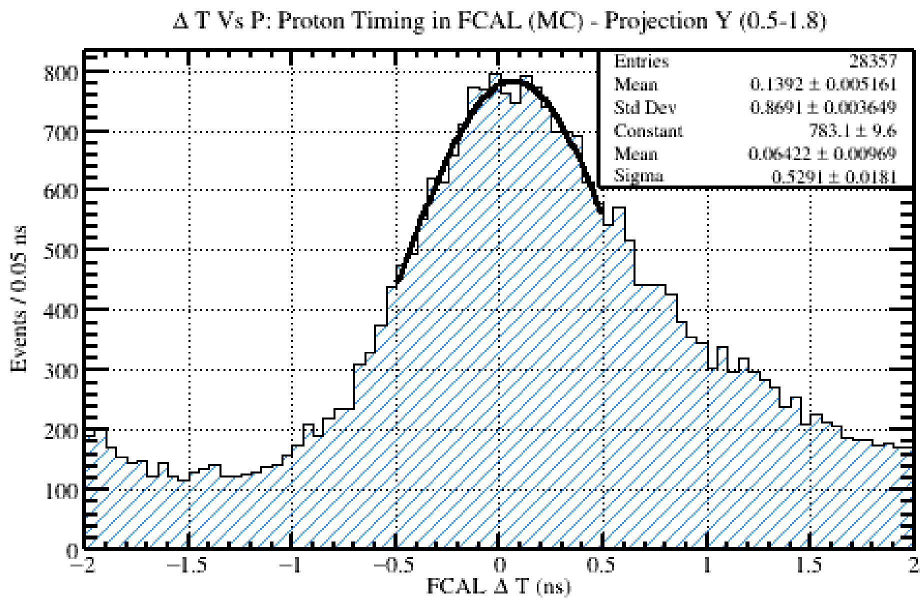

Figure 30: A projection of the statistics from Figure [29] onto the vertical (timing) axis between the momentum range of 0.5-1.8 GeV/C. This projection range was chosen so that the distortion from the lower kaon band was minimized. A Gaussian fit was performed and is included in the figure where the mean and width of the distribution are given in the legend.

be detected by either the Forward Calorimeter or the Barrel Calorimeter and most of these photons appear in the forward direction, it is clear that FCAL showers are causing these photons to appear.

The reconstructed invariant mass for a given $\gamma\gamma$ combination within an event as a function of the number of photons reconstructed within an event can also be shown. By using our Monte Carlo samples, we can also separate these plots into thrown and secondary photons, identical to what we did in Figure [52]. The reconstructed invariant mass of two photons versus the number of reconstructed photons in an event is given in Figure [53]. There are two important observations that should be taken away from the two sub figures. In Figure 53a a clear η resonance can be seen which spans a large number of reconstructed photons per event. What this sub figure tells us right away is that performing a two photon cut on the data is not good for signal events. In fact, after fitting a Gaussian function to the η peaks between 3 and 10 reconstructed photons, it was found that ~8,000 combinations would be lost out of a total of ~30,000; resulting in a 26 percent loss of events. The second important feature seen in Figure 53b is the fact that most of the

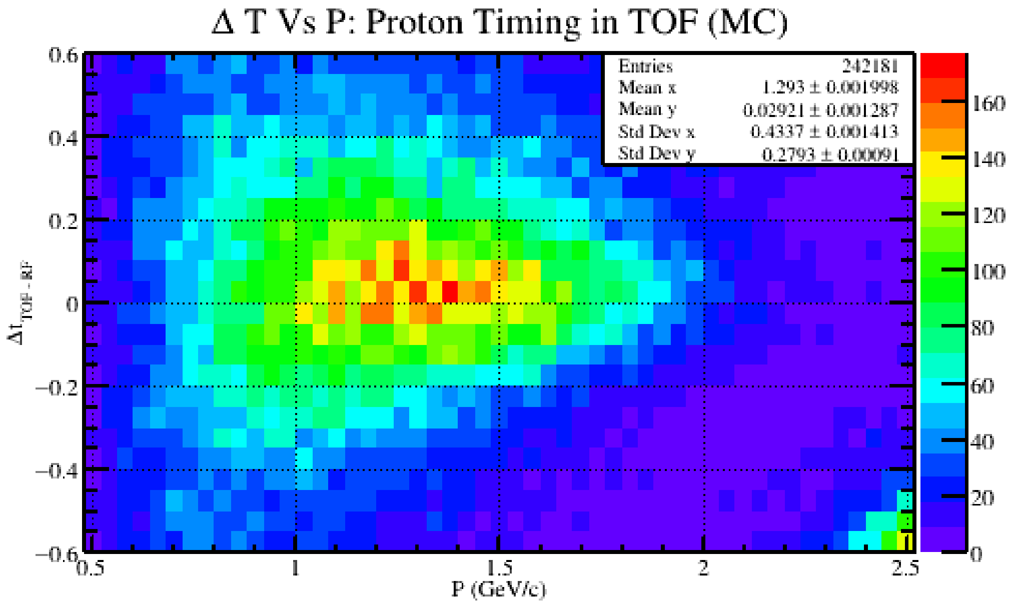

Figure 31: A timing plot for generated protons after reconstruction. The horizontal axis is the reconstructed momentum of the proton and the vertical axis is the timing difference between the TOF and RF. The enhancement of statistics in the lower right portion of the plot comes from miss identified kaons that were also included in the Monte Carlo.

secondary photons exist in events which reconstruct more than two photons per event. Therefore, it is imperative to cut secondary photons while also preserving the event photons that exist in events which yield a large number of reconstructed photons.

There are a number of ways to cut the secondary photons seen in accepted Monte Carlo. The first and most obvious way would be to cut photons that are both below 12° θ and lower than 500 MeV/c in three momentum magnitude. However, since this analysis will eventually include a cut on Kinematic Fit confidence level, the effect of this cut on secondary photons will be studied first. This portion of the study will now include three sets of data: accepted Monte Carlo, background generated Monte Carlo `bggen`, and data. The fist plot that will be shown is the Kinematic Fit confidence level versus the reconstructed $\gamma_1\gamma_2$ invariant mass for all three data sets (Figure [54]). In each plot one can easily see an η peak at higher confidence level along side background which is typically at much lower confidence level. Using the accepted Monte Carlo from Figure [54a] it was determined that a preliminary Kinematic Fit confidence level cut would be placed at the value

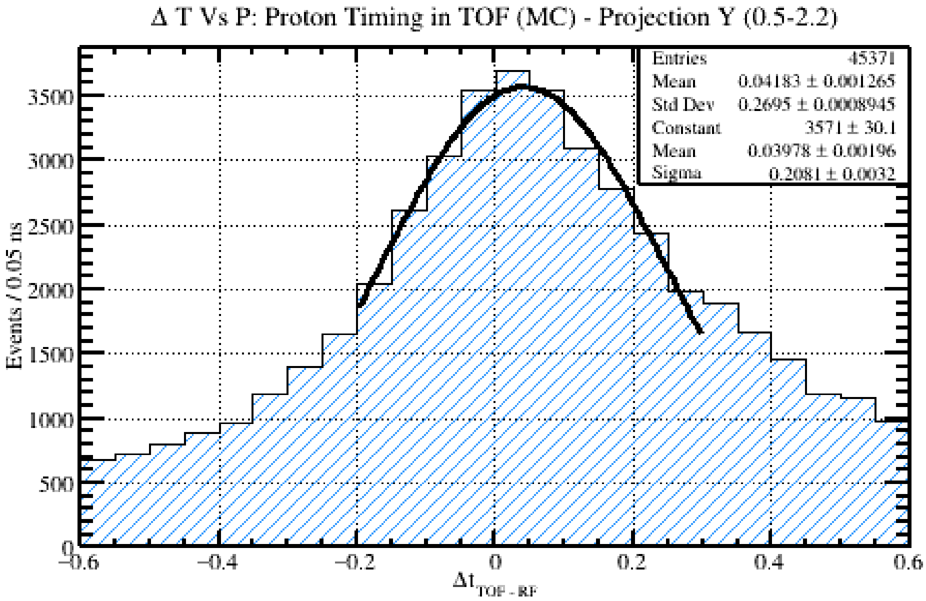

Figure 32: A projection of the statistics from Figure [31] onto the vertical (timing) axis between the momentum range of 0.5-1.8 GeV/C. This projection range was chosen so that the distortion from the lower kaon band was minimized. A gaussian fit was performed and is included in the figure where the mean and width of the distribution are given in the legend.

$1x10^{-6}$.

After performing a confidence level cut of $1x10^{-6}$ it is clear that much of the secondary photons are destroyed. One way of seeing the effect of this cut is by looking at the number of reconstructed photons in an event versus the $\gamma_1\gamma_2$ invariant mass distributions (Figure [55]). Comparing Figure [55a] with Figure [53a], one can easily see that the Kinematic Fit confidence level cut moved many of the η's from high photon reconstruction number per event to low photon reconstruction number per event. This migration of events is due to the fact that the Kinematic Fitter is cutting many secondary photons out of events and therefore decreasing the number of photons reconstructed per event. Furthermore, comparing Figure [55b] with Figure [53b], one can simply look at the density of events within the two dimensional histogram to realize that an overwhelming amount of secondaries has been cut, roughly 94 percent.

Seeing that there is still a non negligible amount of secondary photons left in accepted Monte Carlo and `bggen`, the next cut that will be applied to all of the data is a P Vs θ cut, where $P < 500 MeV/c$ and $\theta < 12$ °. After

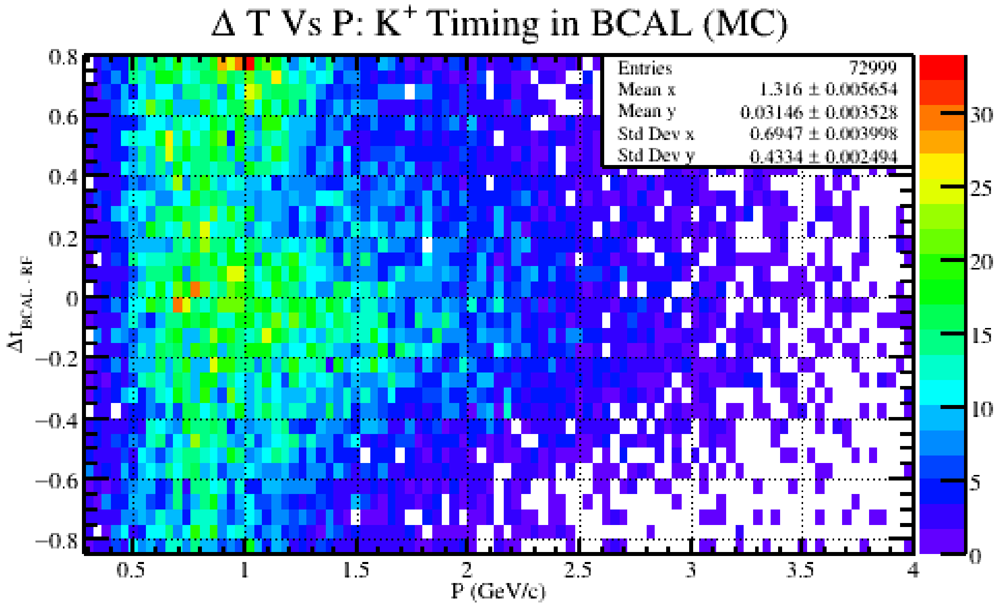

Figure 33: A timing plot for generated K^+ after reconstruction. The horizontal axis is the reconstructed momentum of the K^+ and the vertical axis is the timing difference between the BCAL and RF. It should be noted that the statistics in this sampling are smaller than other plots. This is due to the fact that the kinematics of the generated channel prefer to have the kaons moving in the forwards direction; and therefore provide few timing hits in the BCAL. Additionally, the extra statistics present in the upper left portion of the graph are due to protons included in this Monte Carlo sample.

enforcing these cuts on all photons, the distribution of number of photons reconstructed in an event versus $\gamma_1\gamma_2$ Invariant Mass is shown once again in Figure [56]. It is easy to see that most, if not all of the η signal has migrated to the two photon bin and simultaneously much of the secondary background has been reduced in all data sets. Due to this, a two photon cut is now necessary to do in order to reduce some of the left over background at higher number of reconstructed photons per event.

In this section it was shown that it is necessary to perform a Kinematic Fit confidence level cut; followed by a P Vs θ cut of $P < 500 MeV/c$ and $\theta < 12\,°$; and finally a two photon cut. After completing this sequence of cuts, it was found that 94 percent of background data was cut, while preserving 93 percent of signal data.

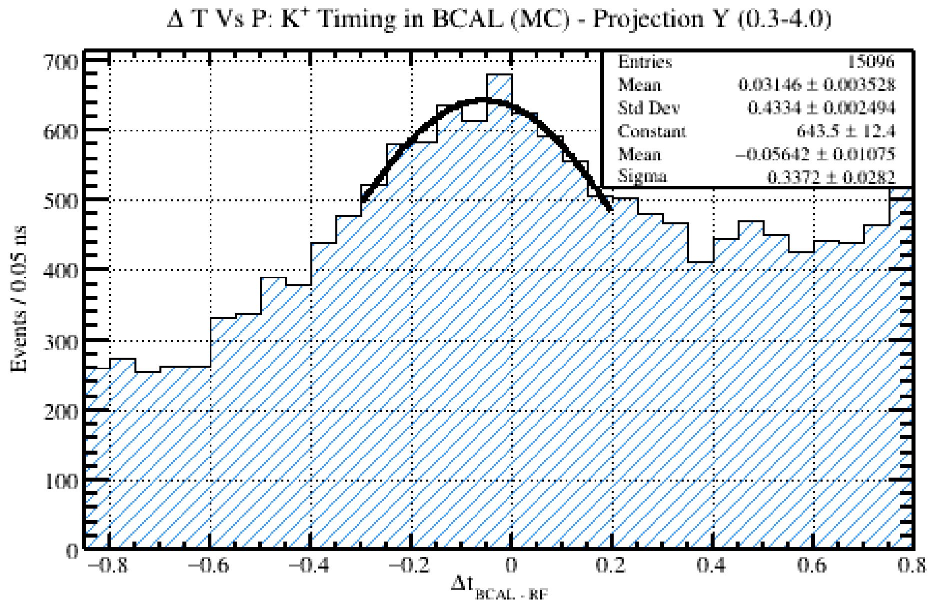

Figure 34: A projection of the statistics from Figure [33] onto the vertical (timing) axis between the momentum range of 0.3-4.0 GeV/C. A Gaussian fit was performed and is included in the figure where the mean and width of the distribution are given in the legend. The distortion of statistics towards the higher timing differences is due to protons included in this Monte Carlo study.

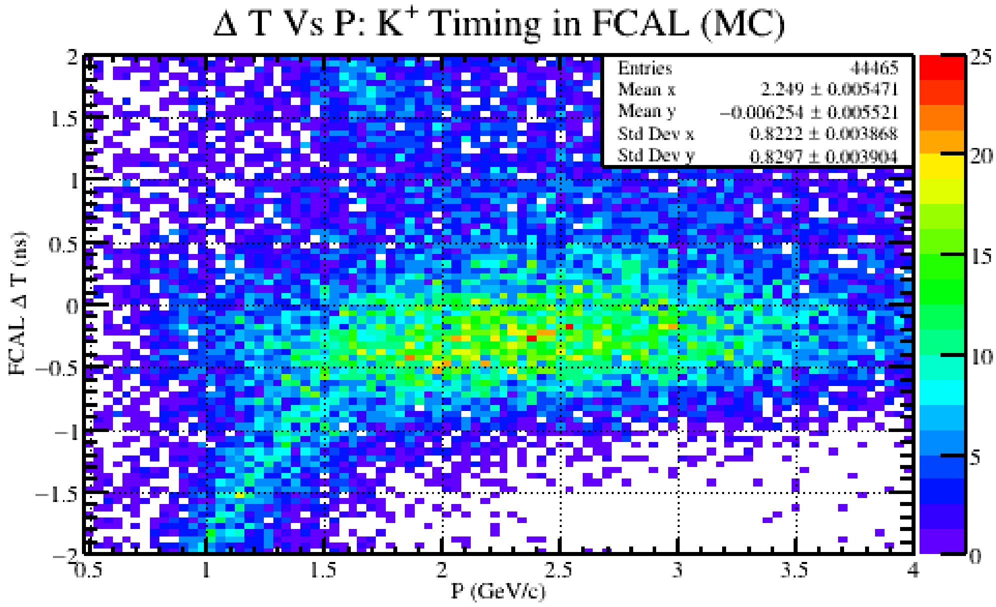

Figure 35: A timing plot for generated K^+ after reconstruction. The horizontal axis is the reconstructed momentum of the K^+ and the vertical axis is the timing difference between the FCAL and RF. The curved band that appears below the K^+ band around 1.5 GeV/c and lower comes from π^+. Although pions were not explicitly generated, the computer program hdgeant (derived from geant) allows for some fraction of kaons to decay weakly while in flight; resulting in an observed pions.

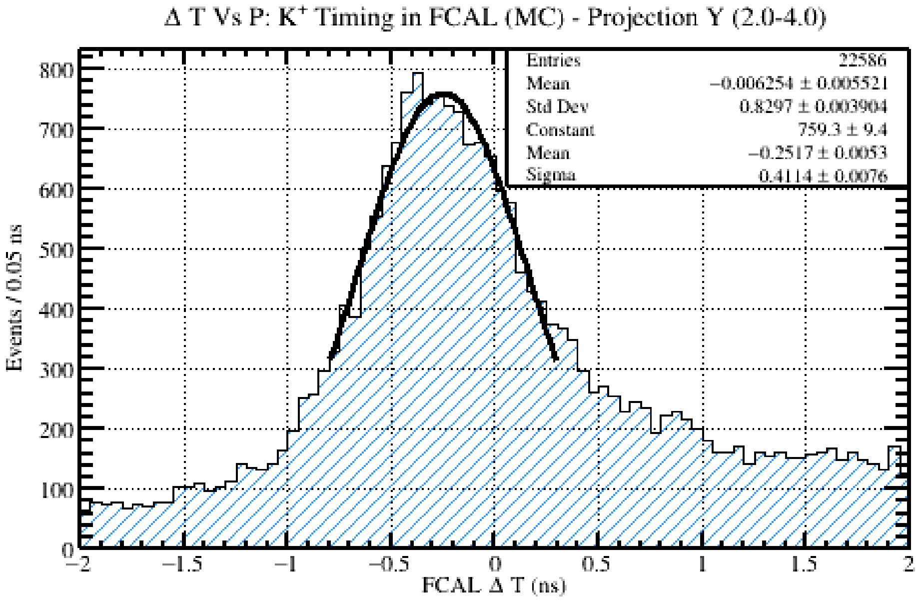

Figure 36: A projection of the statistics from Figure [35] onto the vertical (timing) axis between the momentum range of 2.0-4.0 GeV/C. This projection range was chosen so that the distortion from the lower pion band and upper proton band was minimized. A Gaussian fit was performed and is included in the figure where the mean and width of the distribution are given in the legend.

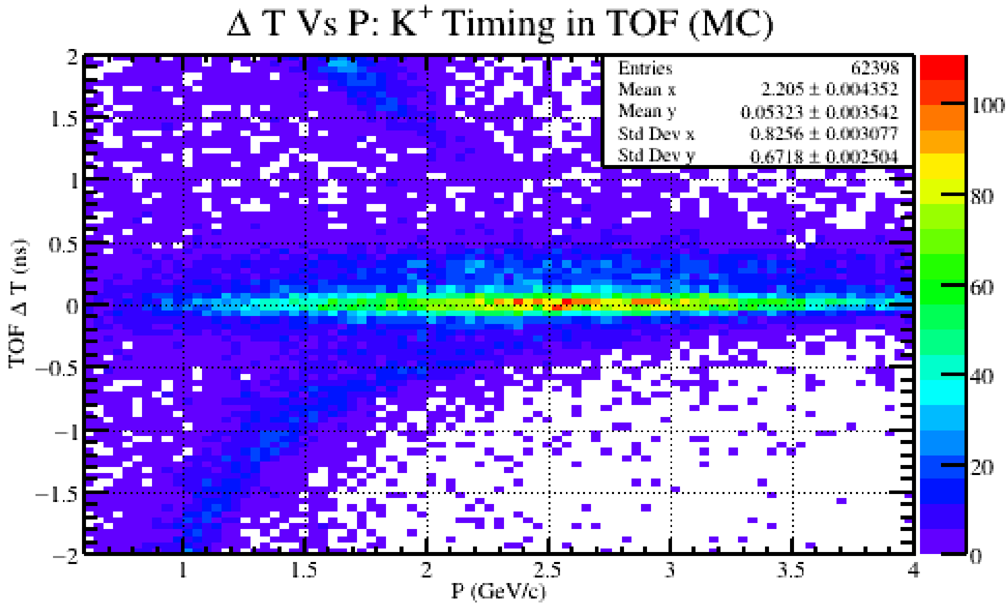

Figure 37: A timing plot for generated K^+ after reconstruction. The horizontal axis is the reconstructed momentum of the K^+ and the vertical axis is the timing difference between the TOF and RF. The curved band that appears below the K^+ band around 2.5 GeV/c and lower comes from π^+; and the band near the top of the plot comes from protons. Although pions were not explicitly generated, the computer program hdgeant (derived from geant) allows for some fraction of kaons to decay weakly while in flight; resulting in an observed pions.

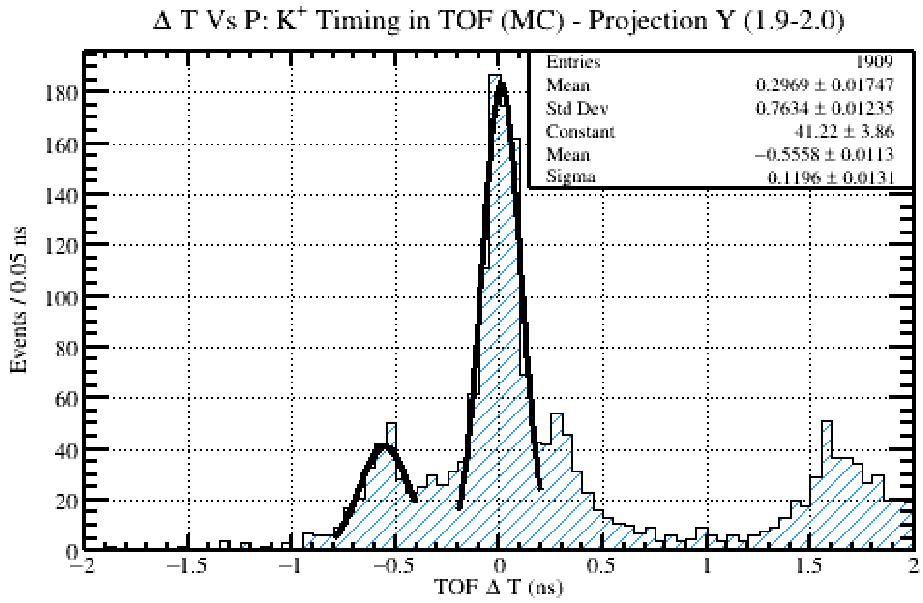

Figure 38: A projection of the statistics from Figure [37] onto the vertical (timing) axis between the momentum range of 1.9-2.0 GeV/C. This projection range is one out of many that were studied from Figure [37]. The purpose of this study is to determine the amount of pion contamination in the kaon band as a function of momentum. The results of this study are provided in Figure [39]. Lastly, two Gaussian fits were performed on this data. The mean and width of these Gaussian fits are recorded in Figure [39] for each momentum range.

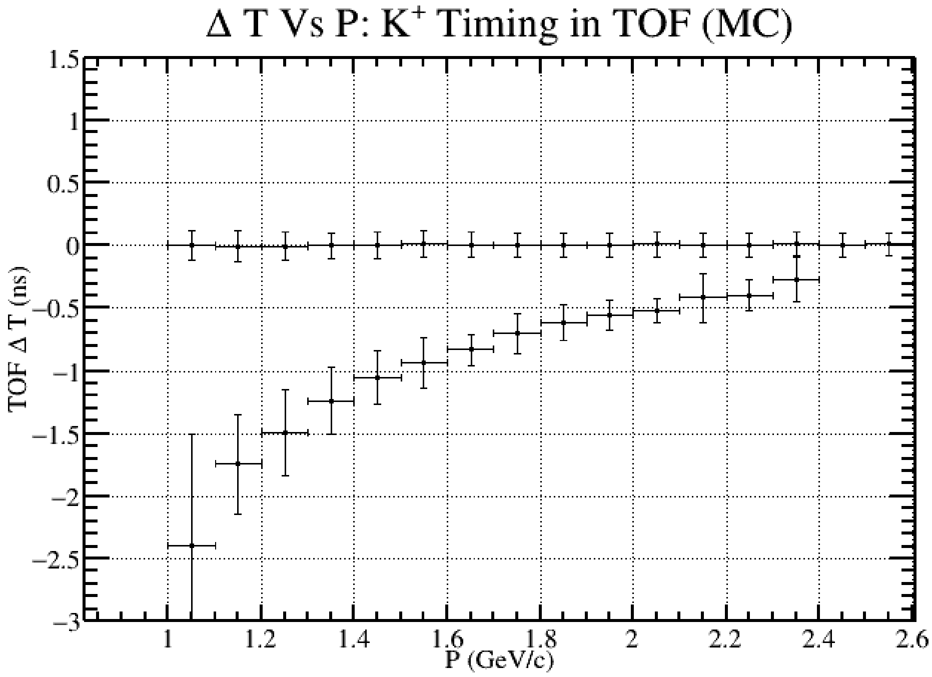

Figure 39: The image above is the result of the timing study performed on Figure [37]. Using that figure, a number of projection histograms were fit using different momentum ranges. An example of one of these fits is given in Figure [38]. The data points close to 0 ΔT correspond to the Gaussian fits performed on the kaon signal, and the data points that approach that band from the bottom correspond to the Gaussian fits performed on the pion signal. The horizontal position of each point is in the middle of the projection range, and the vertical position of each point was assigned based on the mean value of the Gaussian fit for each particle. The horizontal error bars are the size of the projection range, which is always 0.1 GeV/c. The vertical error bars are determined by the width of the Gaussian fits. The average of the widths of the kaon peaks is $0.1ns$ which is the value used to determine the timing cut in Table 1.

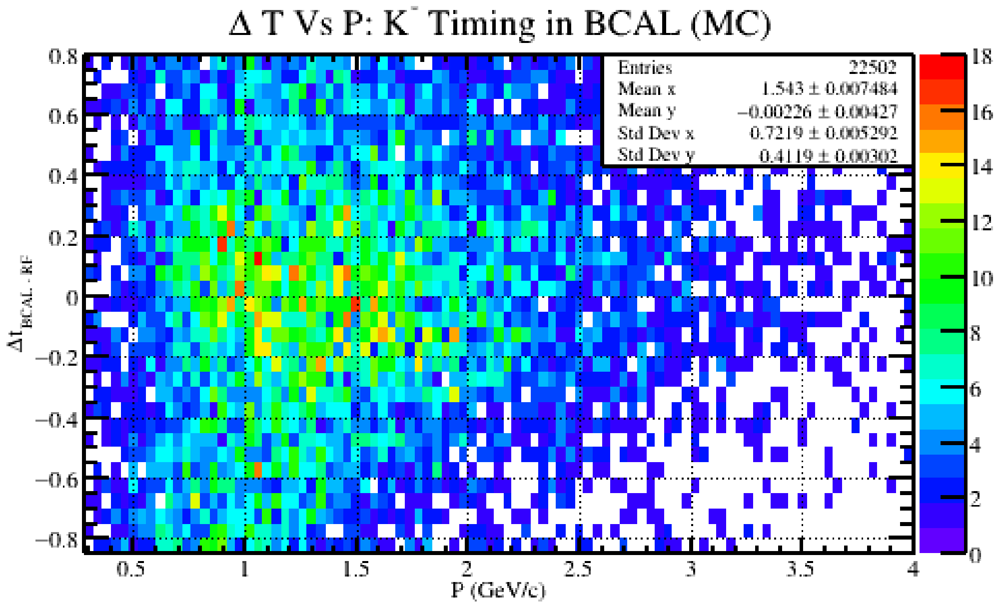

Figure 40: A timing plot for generated K^- after reconstruction. The horizontal axis is the reconstructed momentum of the K^- and the vertical axis is the timing difference between the BCAL and RF. It should be noted that the statistics in this sampling are smaller than other plots. This is due to the fact that the kinematics of the generated channel prefer to have the kaons moving in the forwards direction; and therefore provide few timing hits in the BCAL. Additionally, the extra statistics present in the lower left portion of the graph are due to pions. Although pions were not explicitly generated, the computer program hdgeant (derived from geant) allows for some fraction of kaons to decay weakly while in flight; resulting in an observed pions.

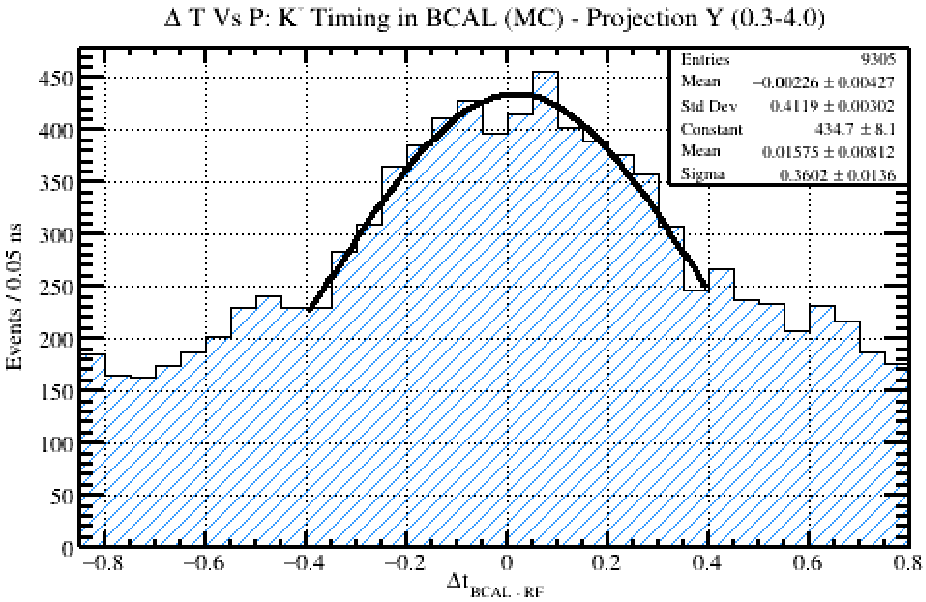

Figure 41: A projection of the statistics from Figure [40] onto the vertical (timing) axis between the momentum range of 0.3-4.0 GeV/C. A Gaussian fit was performed and is included in the figure where the mean and width of the distribution are given in the legend.

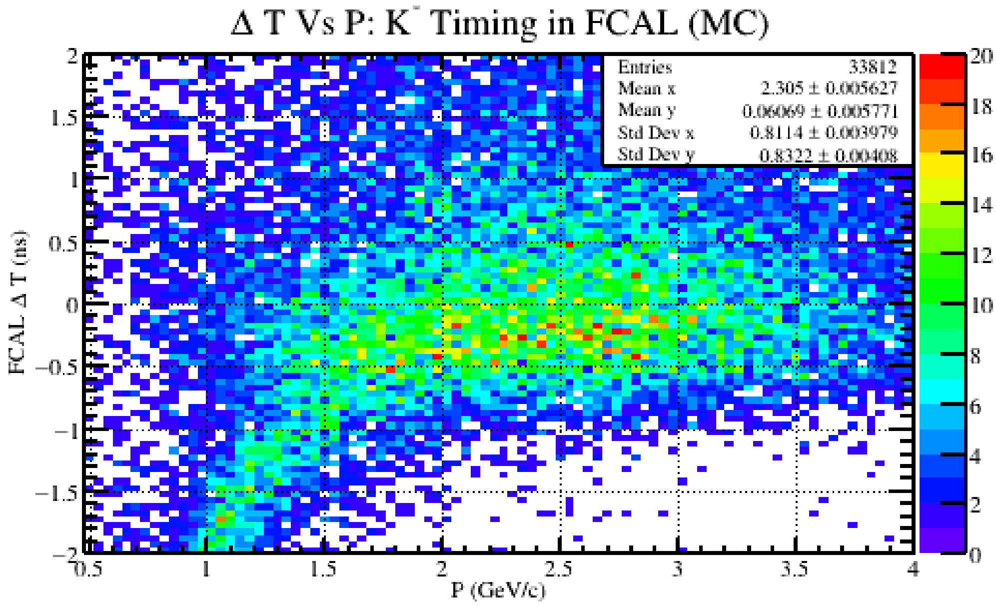

Figure 42: A timing plot for generated K^- after reconstruction. The horizontal axis is the reconstructed momentum of the K^- and the vertical axis is the timing difference between the FCAL and RF. The curved band that appears below the K^- band around 1.5 GeV/c and lower comes from π^-. Although pions were not explicitly generated, the computer program hdgeant (derived from geant) allows for some fraction of kaons to decay weakly while in flight; resulting in an observed pions.

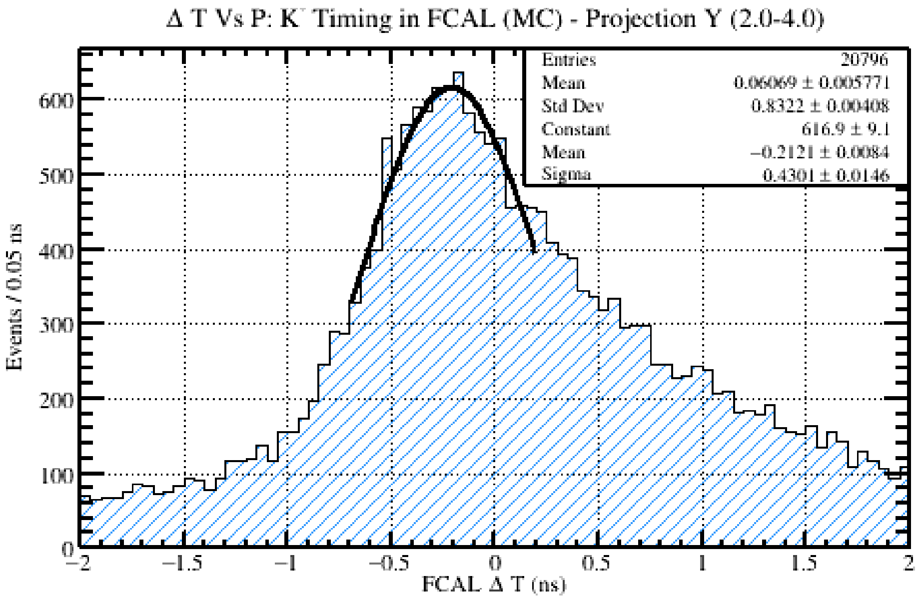

Figure 43: A projection of the statistics from Figure [42] onto the vertical (timing) axis between the momentum range of 2.0-4.0 GeV/C. This projection range was chosen so that the distortion from the lower pion band was minimized. A Gaussian fit was performed and is included in the figure where the mean and width of the distribution are given in the legend.

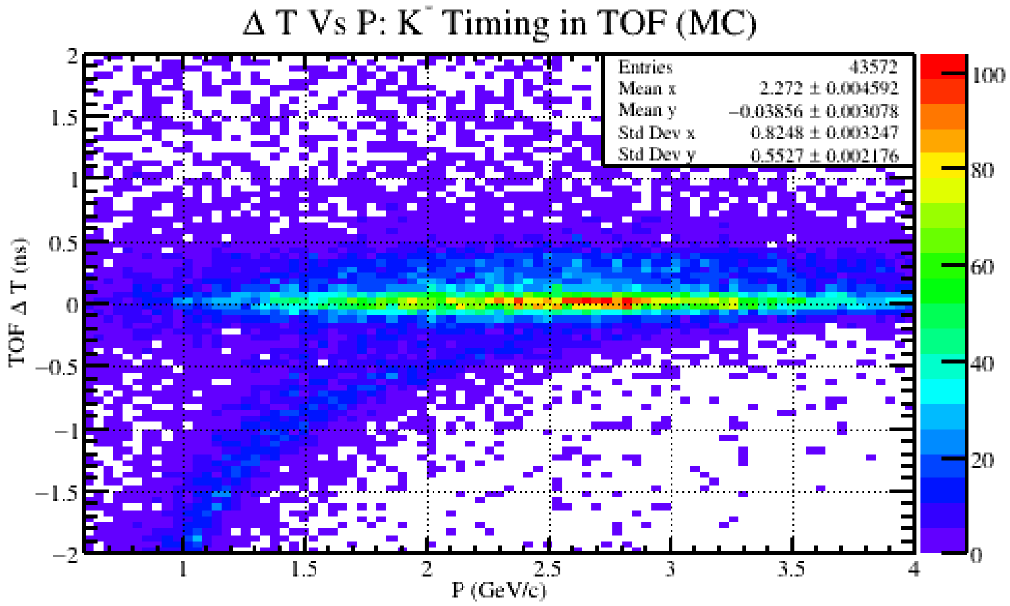

Figure 44: A timing plot for generated K^- after reconstruction. The horizontal axis is the reconstructed momentum of the K^- and the vertical axis is the timing difference between the TOF and RF. The curved band that appears below the K^- band around 2.5 GeV/c and lower comes from π^-. Although pions were not explicitly generated, the computer program hdgeant (derived from geant) allows for some fraction of kaons to decay weakly while in flight; resulting in an observed pions.

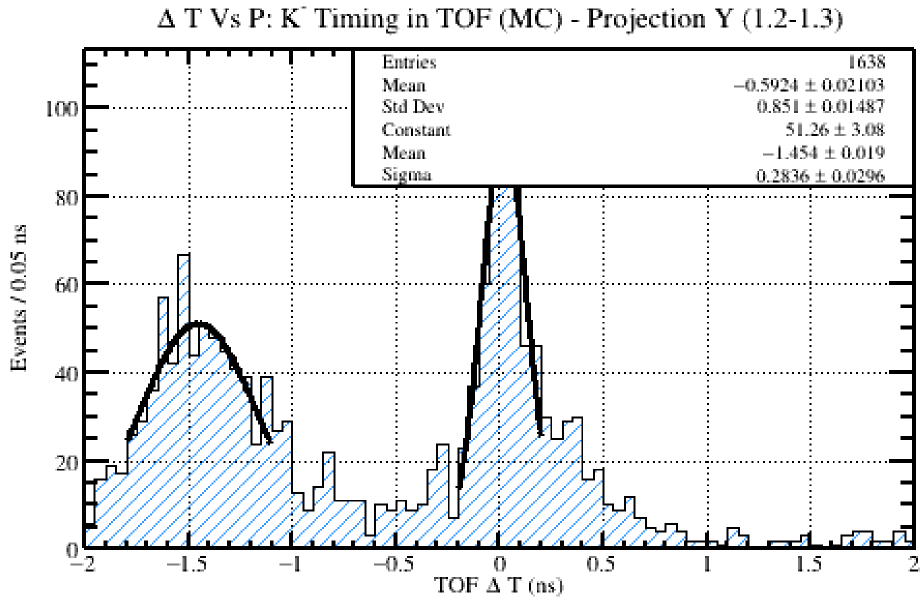

Figure 45: A projection of the statistics from Figure [44] onto the vertical (timing) axis between the momentum range of 1.2-1.3 GeV/C. This projection range is one out of many that were studied from Figure [44]. The purpose of this study is to determine the amount of pion contamination in the kaon band as a function of momentum. The results of this study are provided in Figure [46]. Lastly, two Gaussian fits were performed on this data. The mean and width of these Gaussian fits are recorded in Figure [46] for each momentum range.

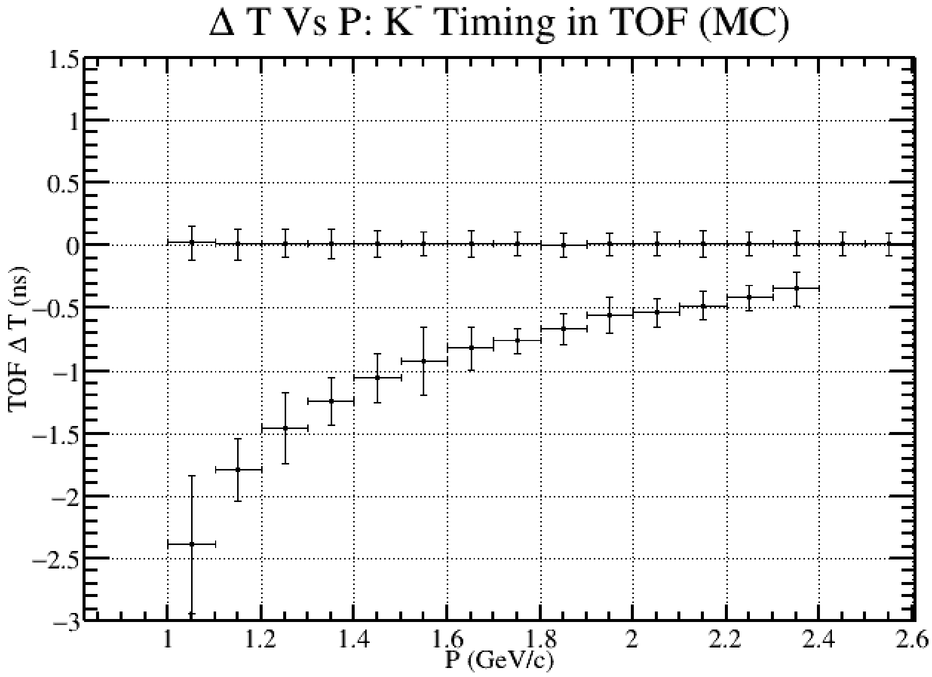

Figure 46: The image above is the result of the timing study performed on Figure [44]. Using that figure, a number of projection histograms were fit using different momentum ranges. An example of one of these fits is given in Figure [45]. The data points close to 0 ΔT correspond to the Gaussian fits performed on the kaon signal, and the data points that approach that band from the bottom correspond to the Gaussian fits performed on the pion signal. The horizontal position of each point is in the middle of the projection range, and the vertical position of each point was assigned based on the mean value of the Gaussian fit for each particle. The horizontal error bars are the size of the projection range, which is always 0.1 GeV/c. The vertical error bars are determined by the width of the Gaussian fits. The average of the widths of the kaon peaks is $0.1ns$ which is the value used to determine the timing cut in Table 1.

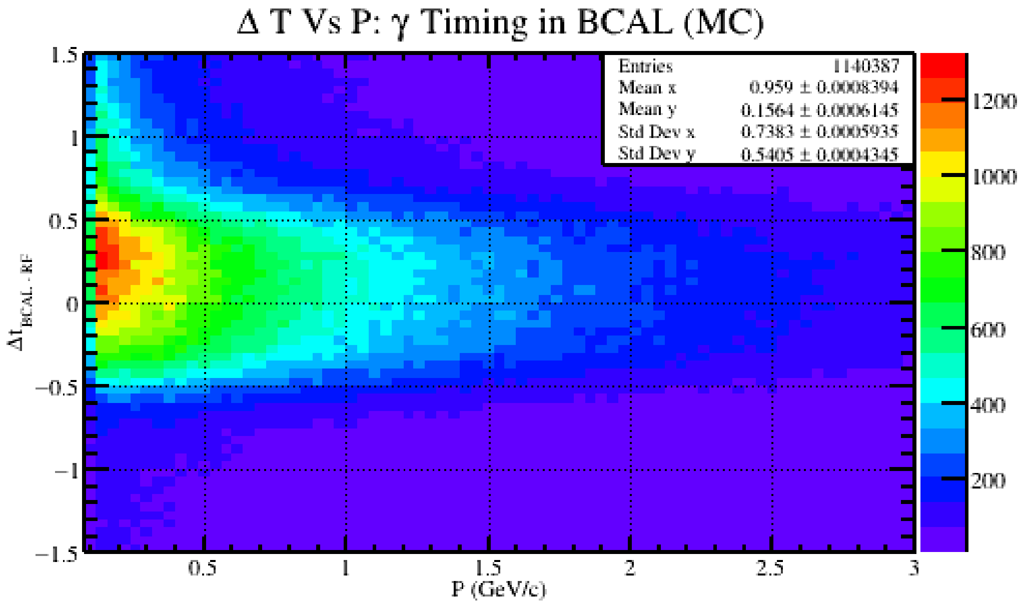

Figure 47: A timing plot for generated γ after reconstruction. The horizontal axis is the reconstructed momentum of the γ and the vertical axis is the timing difference between the BCAL and RF.

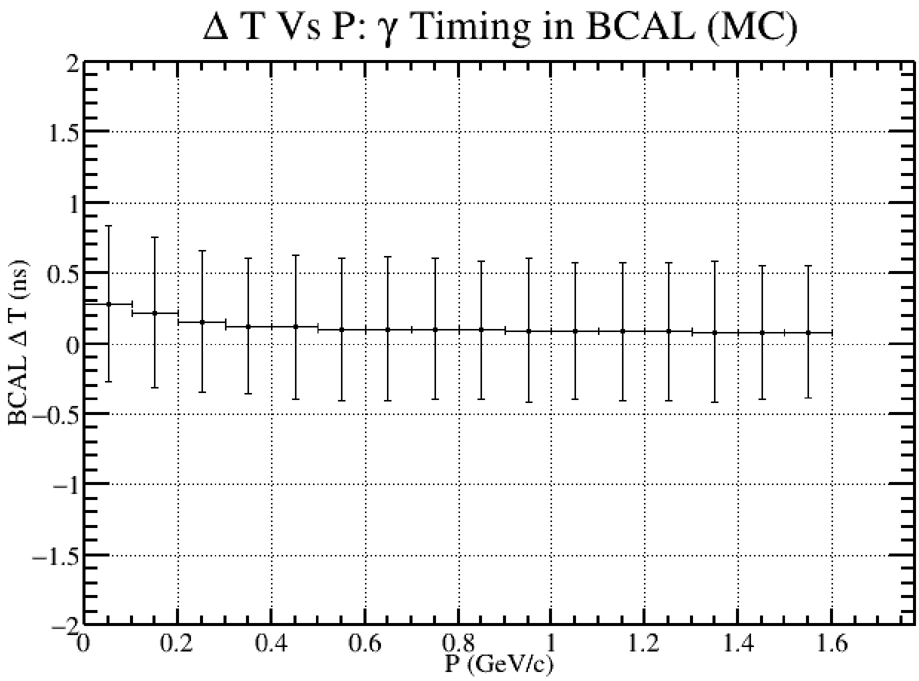

Figure 48: The image above is the result of the timing study performed on Figure [47]. Using that figure, a number of projection histograms were fit using different momentum ranges. The horizontal position of each point is in the middle of the projection range, and the vertical position of each point was assigned based on the mean value of the Gaussian fit. The horizontal error bars are the size of the projection range, which is always 0.1 GeV/c. The vertical error bars are determined by the width of the Gaussian fit. The average of the widths of the photon peaks is $\sim 0.5ns$ which is the value used to determine the timing cut in Table [1].

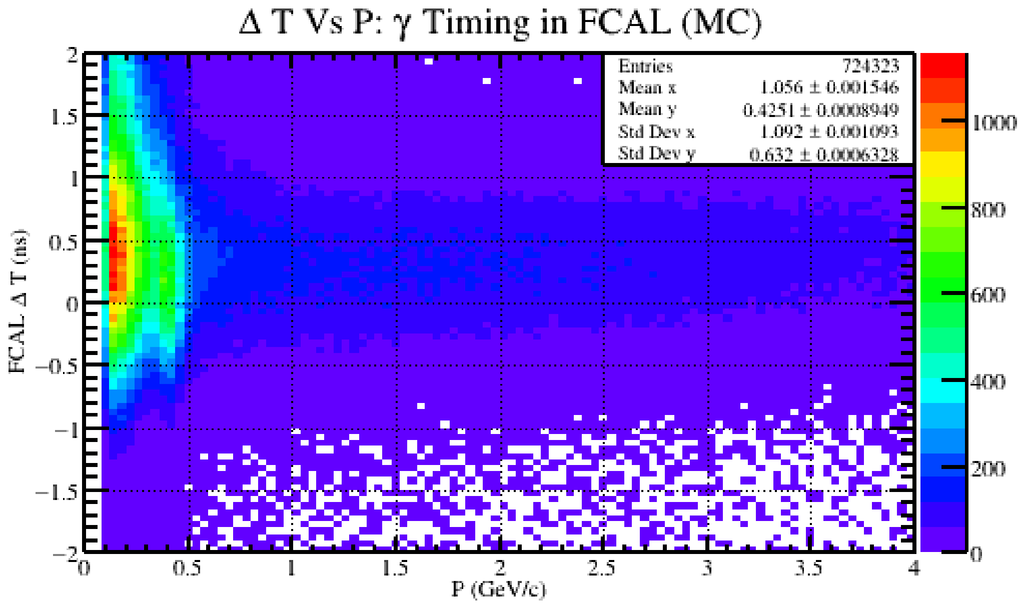

Figure 49: A timing plot for generated γ after reconstruction. The horizontal axis is the reconstructed momentum of the γ and the vertical axis is the timing difference between the FCAL and RF.

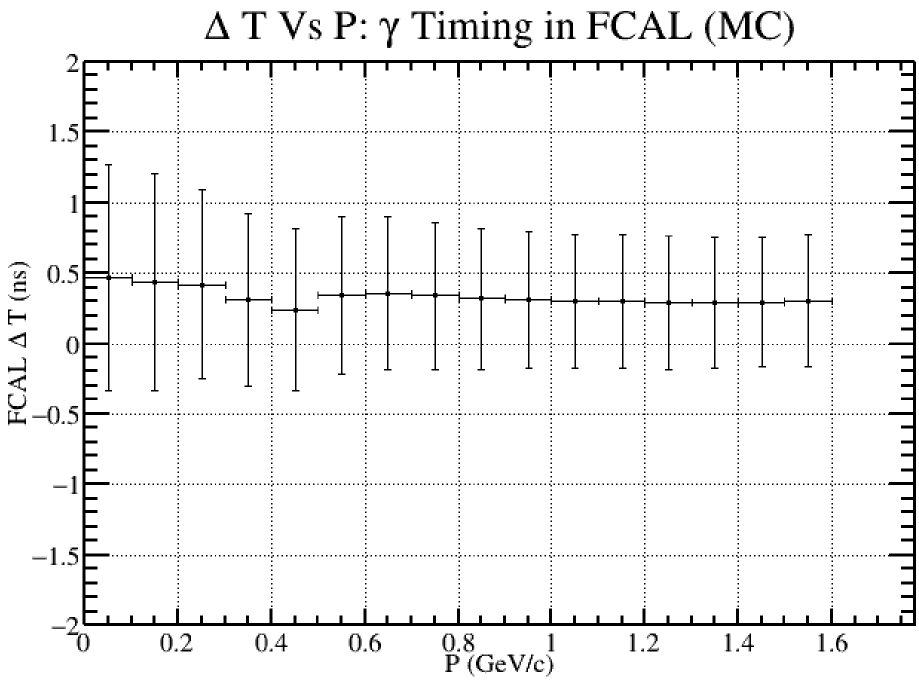

Figure 50: The image above is the result of the timing study performed on Figure [49]. Using that figure, a number of projection histograms were fit using different momentum ranges. The horizontal position of each point is in the middle of the projection range, and the vertical position of each point was assigned based on the mean value of the Gaussian fit. The horizontal error bars are the size of the projection range, which is always 0.1 GeV/c. The vertical error bars are determined by the width of the Gaussian fit. The average of the widths of the photon peaks is $\sim 0.55ns$ which is the value used to determine the timing cut in Table [1].

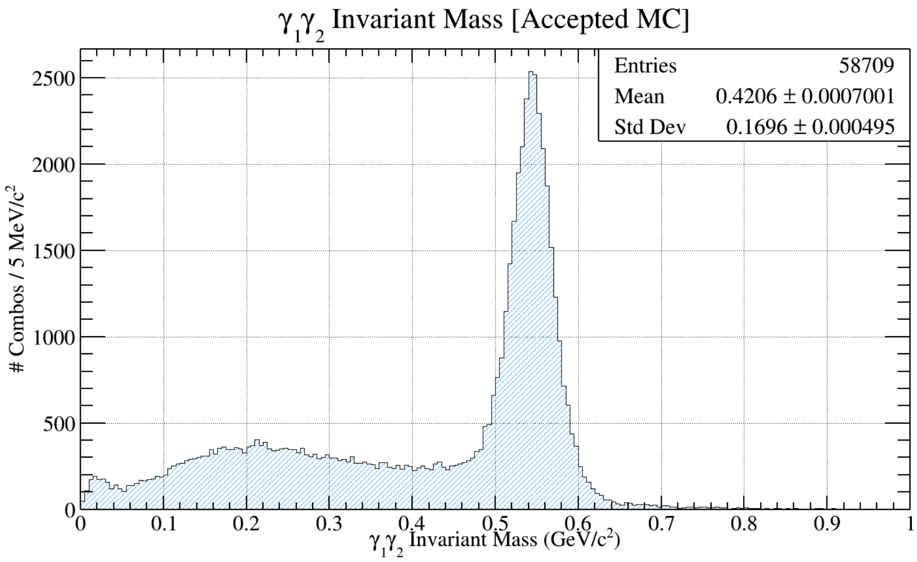

Figure 51: Invariant mass of the reconstructed $\gamma_1\gamma_2$ pair from accepted Monte Carlo. This Monte Carlo data originally came from a $\gamma p \rightarrow p\phi\eta; \phi \rightarrow K^+K^-; \eta \rightarrow \gamma\gamma$ generated topology. An interesting feature of this invariant mass spectra is that it shows a clear η peak, but also contains a background as well. The source of this background is thoroughly studied in subsection 3.3.

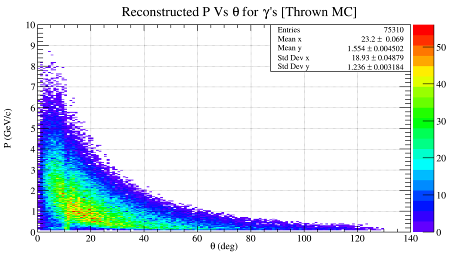

(a) P Vs θ distribution for thrown Monte Carlo photons.

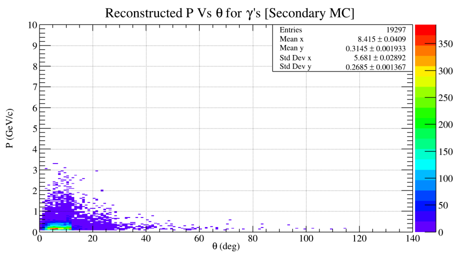

(b) P Vs θ distribution for secondary Monte Carlo photons.

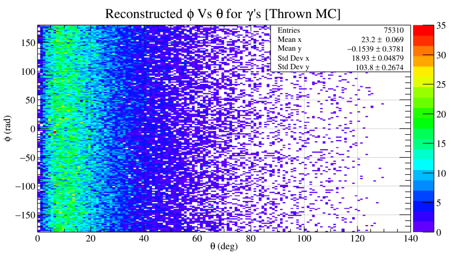

(c) ϕ Vs θ distribution for thrown Monte Carlo photons.

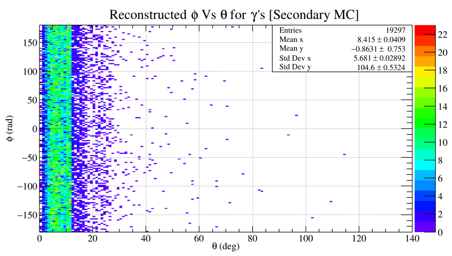

(d) ϕ Vs θ distribution for secondary Monte Carlo photons.

Figure 52: P Vs θ and ϕ Vs θ distributions for thrown (left column) and secondary (right column) photons inside accepted Monte Carlo data.

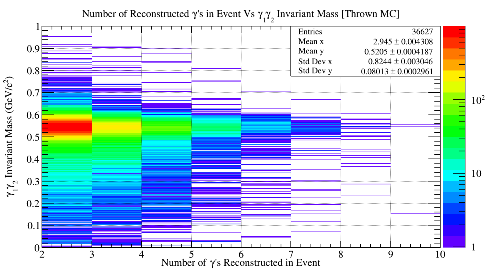

(a) Number of photons reconstructed in an event versus $\gamma_1\gamma_2$ Invariant Mass for thrown photons.

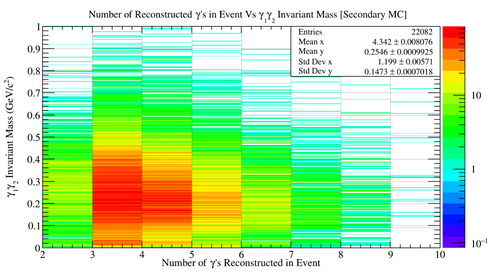

(b) Number of photons reconstructed in an event versus $\gamma_1\gamma_2$ Invariant Mass for secondary photons.

Figure 53: Comparing how the invariant mass for a given $\gamma\gamma$ pair changes depending on the number of reconstructed photons in an event and whether or not the photons were thrown or secondary photons.

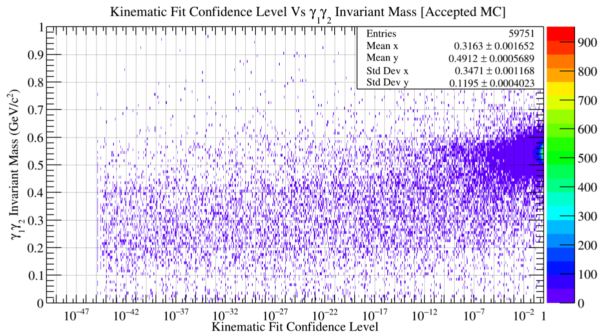

(a) Kinematic Fit confidence level (scaled logarithmically) versus $\gamma_1\gamma_2$ Invariant Mass for accepted Monte Carlo.

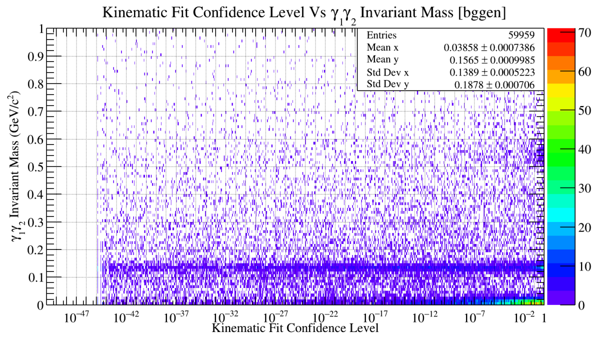

(b) Kinematic Fit confidence level (scaled logarithmically) versus $\gamma_1\gamma_2$ Invariant Mass for background generated Monte Carlo.

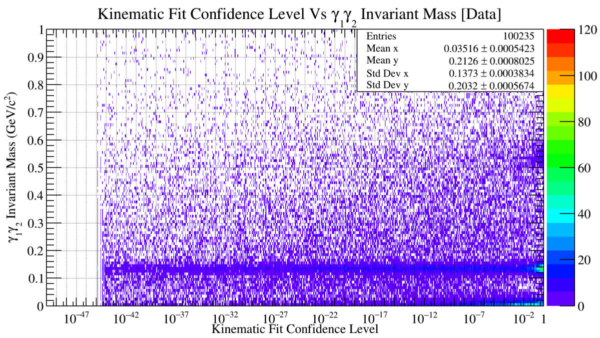

(c) Kinematic Fit confidence level (scaled logarithmically) versus $\gamma_1\gamma_2$ Invariant Mass for data.

Figure 54: Kinematic Fit confidence level (scaled logarithmically) versus $\gamma_1\gamma_2$ Invariant Mass for accepted Monte Carlo, background generated Monte Carlo, and data.

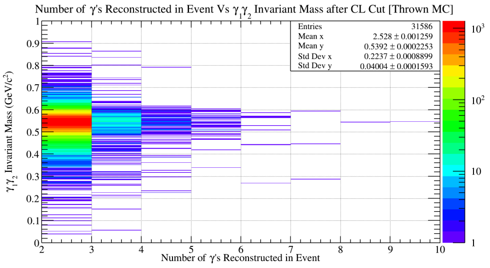

(a) Number of photons reconstructed in an event versus $\gamma_1\gamma_2$ Invariant Mass for thrown photons after a Kinematic Fit confidence level cut of $1x10^{-6}$.

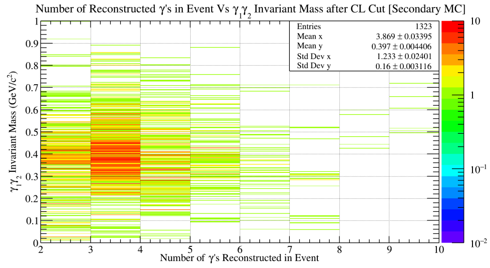

(b) Number of photons reconstructed in an event versus $\gamma_1\gamma_2$ Invariant Mass for secondary photons after a Kinematic Fit confidence level cut of $1x10^{-6}$.

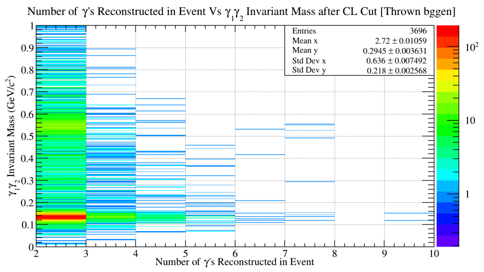

(c) Number of photons reconstructed in an event versus $\gamma_1\gamma_2$ Invariant Mass for thrown photons from `bggen` data after a Kinematic Fit confidence level cut of $1x10^{-6}$.

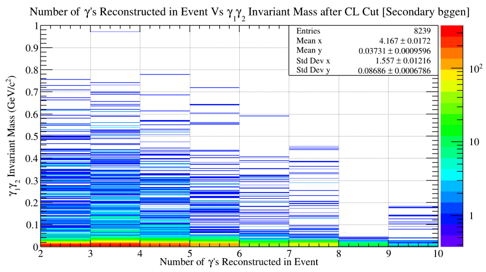

(d) Number of photons reconstructed in an event versus $\gamma_1\gamma_2$ Invariant Mass for secondary photons from `bggen` data after a Kinematic Fit confidence level cut of $1x10^{-6}$.

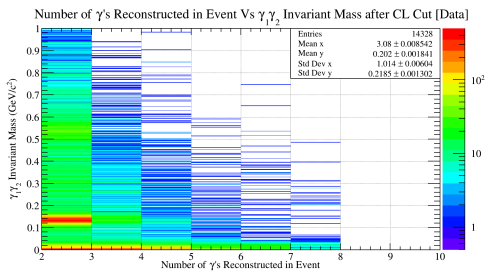

(e) Number of photons reconstructed in an event versus $\gamma_1\gamma_2$ Invariant Mass for data after a Kinematic Fit confidence level cut of $1x10^{-6}$.

Figure 55: Number of photons reconstructed in an event versus $\gamma_1\gamma_2$ Invariant Mass for accepted Monte Carlo, `bggen`, and data after a Kinematic Fit confidence level cut of $1x10^{-6}$.

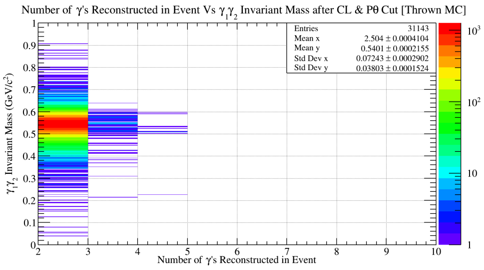

(a) Number of photons reconstructed in an event versus $\gamma_1\gamma_2$ Invariant Mass for thrown photons after a confidence level cut of $1x10^{-6}$ and a P Vs θ cut.

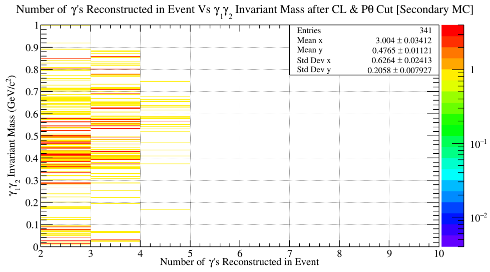

(b) Number of photons reconstructed in an event versus $\gamma_1\gamma_2$ Invariant Mass for secondary photons after a confidence level cut of $1x10^{-6}$ and a P Vs θ cut.

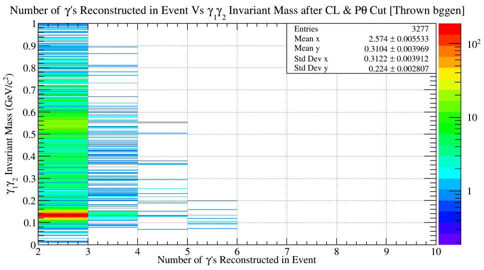

(c) Number of photons reconstructed in an event versus $\gamma_1\gamma_2$ Invariant Mass for thrown photons from `bggen` data after a confidence level cut of $1x10^{-6}$ and a P Vs θ cut.

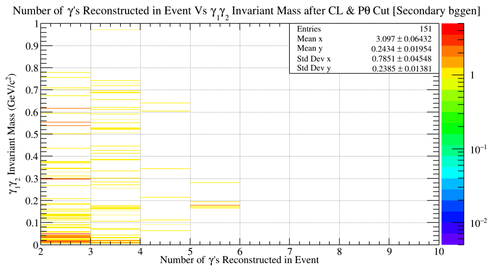

(d) Number of photons reconstructed in an event versus $\gamma_1\gamma_2$ Invariant Mass for secondary photons from `bggen` data after a confidence level cut of $1x10^{-6}$ and a P Vs θ cut.

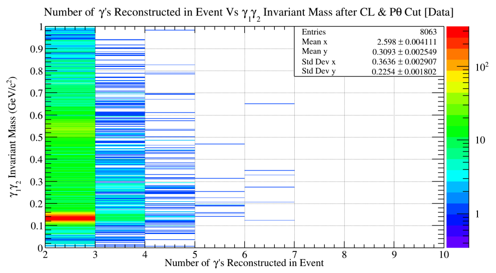

(e) Number of photons reconstructed in an event versus $\gamma_1\gamma_2$ Invariant Mass for data after a confidence level cut of $1x10^{-6}$ and a P Vs θ cut.

Figure 56: Number of photons reconstructed in an event versus $\gamma_1\gamma_2$ Invariant Mass for accepted Monte Carlo, `bggen`, and data after a confidence level cut of $1x10^{-6}$ and a P Vs θ cut.

4 Beam Asymmetry Analysis for $\gamma p \to p\phi\eta$

5 Analysis of $\phi\eta$ Invariant Mass Plot